

PHIBSS: Exploring the Dependence of the CO-H₂ Conversion Factor on Total Mass Surface Density at $z < 1.5$

Timothy Carleton,^{1*} Michael C. Cooper,^{1†}
Alberto D. Bolatto,² Frederic Bournaud,³ Françoise Combes,⁴ Jonathan Freundlich,⁴
Santiago Garcia-Burillo,⁵ Reinhard Genzel,^{6,7,8} Roberto Neri,⁹ Linda J. Tacconi,⁶
Karin M. Sandstrom,¹⁰ Benjamin J. Weiner,¹¹ Axel Weiss¹²

¹Center for Cosmology, Department of Physics and Astronomy, 4129 Reines Hall, University of California, Irvine, CA 92697, USA

²Department of Astronomy, University of Maryland, College Park, MD 20742, USA

³Service d'Astrophysique, DAPNIA, CEA/Saclay, F-91191 Gif-sur-Yvette Cedex, France

⁴LERMA, Observatoire de Paris, CNRS, UPMC, PSL Univ., and College de France, Paris, France

⁵Observatorio Astronómico Nacional (OAN-IGN)-Observatorio de Madrid, Alfonso XII, 3, 28014 Madrid, Spain

⁶Max-Planck-Institut für Extraterrestrische Physik (MPE), Giessenbachstr., D-85748 Garching, Germany

⁷Department of Physics, Le Conte Hall, University of California, Berkeley, CA 94720, USA

⁸Department of Astronomy, Campbell Hall, University of California, Berkeley, CA 94720, USA

⁹IRAM, 300 Rue de la Piscine, F-38406 St. Martin d'Heres, Grenoble, France

¹⁰Center for Astrophysics and Space Sciences, Department of Physics, University of California, San Diego, 9500 Gilman Drive, La Jolla, CA 92093, USA

¹¹Steward Observatory, 933 North Cherry Avenue, University of Arizona, Tucson, AZ 85721, USA

¹²Max Planck Institut für Radioastronomie (MPIfR), Auf dem Hügel 69, 53121 Bonn, Germany

19 December 2016

ABSTRACT

We present an analysis of the relationship between the CO-H₂ conversion factor (α_{CO}) and total mass surface density (Σ_{tot}) in star-forming galaxies at $z < 1.5$. Our sample, which is drawn from the IRAM Plateau de Bure High- z Blue Sequence Survey (PHIBSS) and the CO Legacy Database for GASS (COLD GASS), includes ‘normal,’ massive star-forming galaxies that dominate the evolution of the cosmic star formation rate (SFR) at this epoch and probe the Σ_{tot} regime where the strongest variation in α_{CO} is observed. We constrain α_{CO} via existing CO observations, measurements of the star formation rate, and an assumed molecular gas depletion time ($t_{\text{dep}} = M_{\text{gas}}/\text{SFR}$) — the latter two of which establish the total molecular gas mass independent of the observed CO luminosity. For a broad range of adopted depletion times, we find that α_{CO} is independent of total mass surface density, with little deviation from the canonical Milky Way value. This runs contrary to a scenario in which α_{CO} decreases as surface density increases within the extended clouds of molecular gas that potentially fuel clumps of star formation in $z \sim 1$ galaxies, similar to those observed in local ULIRGs. Instead, our results suggest that molecular gas, both at $z \sim 0$ and $z \sim 1$, is primarily in the form of self-gravitating molecular clouds. While CO observations suggest a factor of ~ 3 reduction in the average molecular gas depletion time between $z \sim 0$ and $z \sim 1$, we find that, for typical galaxies, the structure of molecular gas and the process of star formation at $z \sim 1$ is otherwise remarkably similar to that observed in local star-forming systems.

Key words: galaxies: formation, evolution, high-redshift, ISM, star formation, ISM: molecules

* e-mail: tcarleto@uci.edu

† e-mail: cooper@uci.edu

1 INTRODUCTION

From $z \sim 2$ to today, the volume-averaged cosmic star formation rate (SFR) has declined by an order of magnitude, both globally (Madau et al. 1996; Lilly et al. 1996) and at fixed stellar mass (Noeske et al. 2007; Daddi et al. 2007; Elbaz et al. 2007), driven by a relatively smooth reduction in the star-forming activity of all galaxies rather than a dramatic evolution in the prevalence of mergers or starbursts (Reddy et al. 2008; Magnelli et al. 2011; Madau & Dickinson 2014). This global reduction in star formation is potentially precipitated by either a decrease in the supply of cold gas to galaxies over cosmic time or a lowering in the rate at which gas is converted into stars (i.e. an evolution in star-formation efficiency). To address this question, the Plateau de Bure High- z Blue Sequence Survey (PHIBSS; Tacconi et al. 2010, 2013) measured the molecular gas masses for a sizable sample of typical star-forming galaxies at $z > 1$, finding that cold gas fractions at intermediate redshift are generally a factor of 3 larger, with only a modest evolution in the average star-formation efficiency. Newer studies making use of dust-based gas measurements (Genzel et al. 2015; Santini et al. 2014) and additional CO data from PHIBSS2 (Genzel et al. 2015, Tacconi et al. in prep.) arrive at similar conclusions (see also Papovich et al. 2016). These results suggest that evolution in the cosmic star formation space density stems chiefly from a decrease in the supply of cold gas, with no evidence for substantial evolution in the physics of star formation over the past 7–10 Gyr.

As with all current studies of molecular gas at high redshift, however, the results from PHIBSS rely on the uncertain conversion of an observed molecular line luminosity (or some other indirect tracer) to a measurement of the molecular gas mass. Within local star-forming galaxies, molecular gas is primarily composed of molecular hydrogen (H_2) in giant molecular clouds (GMCs, McKee & Ostriker 2007). Because it lacks a permanent dipole moment to facilitate low energy dipole transitions, and the allowed quadrupole transitions have very low probabilities ($A \sim 10^{-7} \text{ s}^{-1}$) and trace only warm ($T \sim 5,000 \text{ K}$) gas, the H_2 in molecular clouds is nearly invisible via direct emission. Thus, the bright dipole transitions of the next most abundant molecule, carbon monoxide (CO), are frequently used as molecular gas tracers. Extragalactic studies rely heavily on CO emission to determine the molecular gas mass (M_{gas}) from the observed velocity-integrated CO luminosity (L'_{CO}) by way of the CO- H_2 conversion factor, α_{CO} :

$$M_{\text{gas}} = \alpha_{\text{CO}} L'_{\text{CO}}, \quad (1)$$

where M_{gas} (and thus α_{CO}) includes a 36 per cent correction for Helium ($M_{\text{gas}} = M_{H_2} + M_{He} = 1.36 M_{H_2}$).¹ Although CO emission originates from only a fraction of the total molecular gas, for self-gravitating GMCs, α_{CO} is expected to be largely independent of GMC mass, given that both the CO luminosity and molecular gas mass at the CO emitting surface are proportional to the enclosed total mass. In particular, the α_{CO} value of a self-gravitating molecular cloud is proportional to $n^{1/2}/T$ (Dickman, Snell & Schloerb 1986), where n is the gas density and T is the kinetic temperature.

Within the Milky Way, observations arrive at a value of $\alpha_{\text{CO,MW}} = 4.36 M_{\odot} (\text{K km s}^{-1} \text{ pc}^2)^{-1} \pm \sim 30$ per cent across a wide range of GMC properties and environments (e.g. Dickman 1978; Frerking, Langer & Wilson 1982; Ade et al. 2011; Ackermann et al. 2012), indicative of a uniformity in the temperature and density of molecular clouds. As such, the canonical Milky Way

value for α_{CO} is commonly utilized as a constant conversion factor throughout a wide range of extragalactic studies. However, systematic variation of α_{CO} with certain properties of the interstellar medium (ISM, e.g. metallicity) is both expected from theoretical arguments and observed in a number of systems (Leroy et al. 2011; Sandstrom et al. 2013; Strong et al. 2004; Papadopoulos et al. 2012b).

As with other molecular tracers, CO emission originates from gas that is denser and further within molecular clouds than most of the molecular hydrogen, resulting in a shell of H_2 between the CO emitting surface and the edge of the molecular cloud. The size of this shell (and thus the fraction of ‘CO dark’ molecular gas) depends on the efficiency of intervening dust at shielding CO from the galactic radiation field. In this way, low-metallicity clouds with a lower dust-to-gas ratio have higher α_{CO} values. The conversion factor is further coupled to the cloud structure because CO emission is almost always optically thick (Dickman 1978; Solomon et al. 1987), and thus the CO intensity is determined by the temperature and velocity dispersion at the $\tau_{\text{CO}} = 1$ surface within the molecular cloud. Clouds with sources of dispersion beyond self-gravity, such as tidal disruptions or embedded stars, can have brighter CO emission than self-gravitating molecular clouds of the same mass, thus lowering α_{CO} . Observationally, this effect primarily manifests itself as a correlation between α_{CO} and density — molecular clouds in high-density environments tend to be composed of ‘diffuse’ molecular gas containing embedded stars that increase the velocity dispersion beyond that of a self-gravitating cloud. Based on these arguments, α_{CO} is commonly parameterized as a function of the ISM density and temperature times a separate function of metallicity (Bolatto, Wolfire & Leroy 2013; Narayanan et al. 2012; Tacconi et al. 2013). As these ISM characteristics are known to vary with redshift (e.g. Magdis et al. 2012a; Zahid et al. 2013; Carilli & Walter 2013), α_{CO} very likely evolves with cosmic time.

Overall, observations indicate that the Milky Way value of $\alpha_{\text{CO}} = 4.36 M_{\odot} (\text{K km s}^{-1} \text{ pc}^2)^{-1}$ is applicable for most galaxies, signifying a relative uniformity in molecular cloud conditions (Bolatto et al. 2008; Leroy et al. 2011; Sandstrom et al. 2013; Schinnerer et al. 2010). On the other hand, observations within the Milky Way and in a relatively small number of nearby and distant systems show variation in α_{CO} consistent with the expected dependence on ISM conditions described above. For example, variation in α_{CO} with gas-phase metallicity has been observed within the Local Group (Israel 1997; Leroy et al. 2011), nearby galaxies (Sandstrom et al. 2013), and even a handful of systems at $z > 1$ (Genzel et al. 2012). While these results are all consistent with α_{CO} increasing by over an order of magnitude for metallicities less than 30 per cent solar, measurements of α_{CO} at a fixed metallicity have a large dispersion, especially in medium-to-high metallicity environments (Sandstrom et al. 2013).

Variation in α_{CO} with mass surface density has also been observed in the Milky Way, with γ -ray, dust, and dynamical observations of the dense Galactic center arriving at a lower α_{CO} than that found in the solar neighborhood (Sodroski et al. 1995; Oka et al. 2001; Strong et al. 2004). Recent dust-based measurements of α_{CO} within nearby galaxies find a similar decrease in α_{CO} at small galactic radii (Sandstrom et al. 2013). Moreover, for over a decade, it has been known that the star-forming centers of Ultra-Luminous Infrared Galaxies (ULIRGs, Aaronson & Olszewski 1984) require a lower α_{CO} in order for their CO luminosities to be consistent with their dynamical masses (Downes & Solomon 1998). As a result, a lower value of $\alpha_{\text{CO}} = 0.8 M_{\odot} (\text{K km s}^{-1} \text{ pc}^2)^{-1}$ is commonly adopted for mergers and ULIRGs (Solomon et al. 1997; Downes &

¹ Alternatively, the conversion factor (X_{CO}) can be defined in terms of column density, such that $N_{H_2} = X_{\text{CO}} L_{\text{CO}}$.

Solomon 1998; Tacconi et al. 2006, 2008; Krumholz & Thompson 2007; Daddi et al. 2010).

At high redshift, where molecular gas conditions may differ from those locally, most measurements of α_{CO} have been biased towards massive, highly star-forming galaxies that are not representative of the typical star-forming environment at high z (e.g. Tacconi et al. 2008; Magdis et al. 2011; Spilker et al. 2015). In the new era of high-sensitivity radio telescopes, such as the Northern Extended Millimeter Array (NOEMA) and the Atacama Large Millimeter Array (ALMA), it is possible to probe molecular gas conditions at $z \gtrsim 2$ via CO (e.g. Ivison et al. 2012; Wang et al. 2013; Tamura et al. 2014; Messias et al. 2014; Béthermin et al. 2016). In order for these observations to provide insight into the evolution of cosmic star-formation activity since $z \gtrsim 1$, a better understanding of α_{CO} and its dependence on galaxy properties for typical high- z systems is critical. Motivated by the dependence of α_{CO} on ISM properties observed locally, we study variations in α_{CO} with integrated galaxy properties, in particular mass surface density, in 38 massive star-forming galaxies at $z = 1 - 1.5$ and a comparison sample of 164 systems at $z \sim 0.05$. In Section 2, we detail our observational datasets and galaxy samples. Section 3 describes the technique that we use for measuring α_{CO} , while Section 4 summarizes our results regarding the relationship between α_{CO} and mass surface density. Finally, Sections 5 and 6 contain a discussion regarding the implications of our results and as well as itemized conclusions. Throughout this paper, we adopt a Chabrier (2003) initial mass function and a Λ CDM cosmology with $H_0 = 70 \text{ km s}^{-1} \text{ Mpc}^{-1}$, $\Omega_M = 0.3$, and $\Omega_\Lambda = 0.7$.

2 DATA

2.1 High- z Sample

Our high- z galaxy sample includes 38 star-forming systems at $1 < z < 1.5$ from the IRAM Plateau de Bure High- z Blue Sequence Survey (PHIBSS; Tacconi et al. 2010, 2013). PHIBSS is one of the largest high-redshift surveys of molecular gas to date, observing CO emission from massive star-forming galaxies at $z = 1.0 - 1.5$ and $z = 2 - 2.5$ with the IRAM Plateau de Bure interferometer. The PHIBSS sample at $1 < z < 1.5$ is selected from the All-Wavelength Extended Growth Strip International Survey (AEGIS; Davis et al. 2007), which provides extensive multiwavelength imaging, including V_{F606W} - and I_{F814W} -band observations with the *Hubble Space Telescope* (*HST*) Advanced Camera for Surveys (ACS) and spectroscopic redshifts from the DEEP2 and DEEP3 Galaxy Redshift Surveys for each galaxy (Newman et al. 2013; Cooper et al. 2011, 2012; Lotz et al. 2008). In addition, J_{F125W} - and H_{F160W} -band *HST*/WFC3-IR imaging from the Cosmic Assembly Near-infrared Deep Extragalactic Legacy Survey (CANDELS; Grogin et al. 2011; Koekemoer et al. 2011; van der Wel et al. 2014) covers 32 of the 38 PHIBSS galaxies, while *HST*/WFC3-IR G141 grism observations exist for 28 of the 38 systems in our high- z sample (see Section 2.4).

At $1 < z < 1.5$, PHIBSS targets ‘normal’ star-forming galaxies, probing down to star formation rates of $30 \text{ M}_\odot \text{ yr}^{-1}$ and a stellar mass limit of $2.5 \times 10^{10} \text{ M}_\odot$. This high- z sample has a median stellar mass of $6.7 \times 10^{10} \text{ M}_\odot$, within 0.2 dex of M^* at this redshift (Ilbert et al. 2010), and a median star formation rate of $87 \text{ M}_\odot \text{ yr}^{-1}$, corresponding to a sample predominantly composed of Luminous Infrared Galaxies (LIRGs; Sanders & Mirabel 1996). As shown in Figure 1, all galaxies sit on or slightly above the ‘star-forming main sequence’, where the majority of star formation occurs (e.g. Noeske

et al. 2007; Rodighiero et al. 2011; Speagle et al. 2014; Whitaker et al. 2012). Only 11 per cent of the galaxies are more than 0.6 dex above the main sequence, and the median difference between the sample and the main sequence (taken from Whitaker et al. 2012) is 0.3 dex.

Although there is no size or morphological consideration in the selection, we ensure that the size distribution of PHIBSS is representative of typical high- z star formers, utilizing a control sample of star-forming galaxies at $1 \leq z \leq 1.5$ from the Advanced Camera for Surveys–General Catalog (ACS-GC; Griffith et al. 2012) and the RAINBOW database (Barro et al. 2011).² The control sample is restricted to galaxies with $\text{SFR} > 30 \text{ M}_\odot \text{ yr}^{-1}$, stellar mass uncertainty < 0.5 dex and I -band surface brightness profiles that can be reliably fit with a one-component Sérsic profile (GALFIT_FLAG=0). From this parent sample (shown in Figure 2), we build a mass-matched distribution by randomly drawing (with replacement) 1000 galaxies with stellar masses within 0.3 dex of each PHIBSS object. Using this selection, 88 per cent of PHIBSS galaxies are within the central two quartiles of the size distribution of the control sample, indicating that our high- z sample is not particularly biased toward compact or diffuse systems.

Perhaps more importantly, it is unlikely that the PHIBSS sample is biased towards abnormally gas-rich or gas-poor objects. While there is no reference sample at $z \sim 1$, to which to compare the observed gas fractions, all of the PHIBSS *targets* at $z \sim 1$ are detected in CO emission and reside near the star-forming main sequence at this redshift. Thus, there is no reason to believe that the 10 – 80 per cent gas fractions detected in PHIBSS are not representative.

2.2 Low- z Sample

As a low-redshift comparison sample, with which to study potential evolution in α_{CO} , we utilize data from the CO Legacy Database for GASS (COLD GASS; Saintonge et al. 2011a) along with published α_{CO} measurements from the literature (Sandstrom et al. 2013; Leroy et al. 2011; Papadopoulos et al. 2012a). COLD GASS is an extension of the *GALEX* Arecibo SDSS Survey (GASS; Catinella et al. 2010), which measured H I gas masses for an unbiased, stellar mass-selected sample of galaxies at $0.025 < z < 0.05$ drawn from the Sloan Digital Sky Survey (SDSS; York et al. 2000). As the largest molecular gas survey in the local Universe, COLD GASS provides an excellent comparison dataset at low redshift, probing a stellar mass range comparable to that of our high- z sample.

Similar to PHIBSS, COLD GASS targets galaxies with stellar masses ranging from $10^{10} - 10^{11.5} \text{ M}_\odot$, with a median value of $10^{10.5} \text{ M}_\odot$. Unlike PHIBSS, however, COLD GASS targets both quiescent and star-forming galaxies. To avoid including galaxies with a potentially distinct star-formation process in our analysis, we exclude quenched galaxies, defined as systems with

$$\log \left(\frac{\text{SFR}}{\text{M}_\odot \text{ yr}^{-1}} \right) \leq 0.44 \log \left(\frac{M_*}{\text{M}_\odot} \right) - 5.29. \quad (2)$$

This division is determined by a linear fit to the minimum of the distribution of galaxies at $z < 0.05$ in the $\log \text{sSFR} - \log M_*$ plane and is shown as the dashed line in Fig. 1b. Further limiting our analysis to objects with a CO detection only eliminates 15 of the 179 star-forming galaxies, leaving 164 in our final sample. These cuts generate a sample similar to PHIBSS that is largely unbiased in terms

² <http://rainbowx.fis.ucm.es>

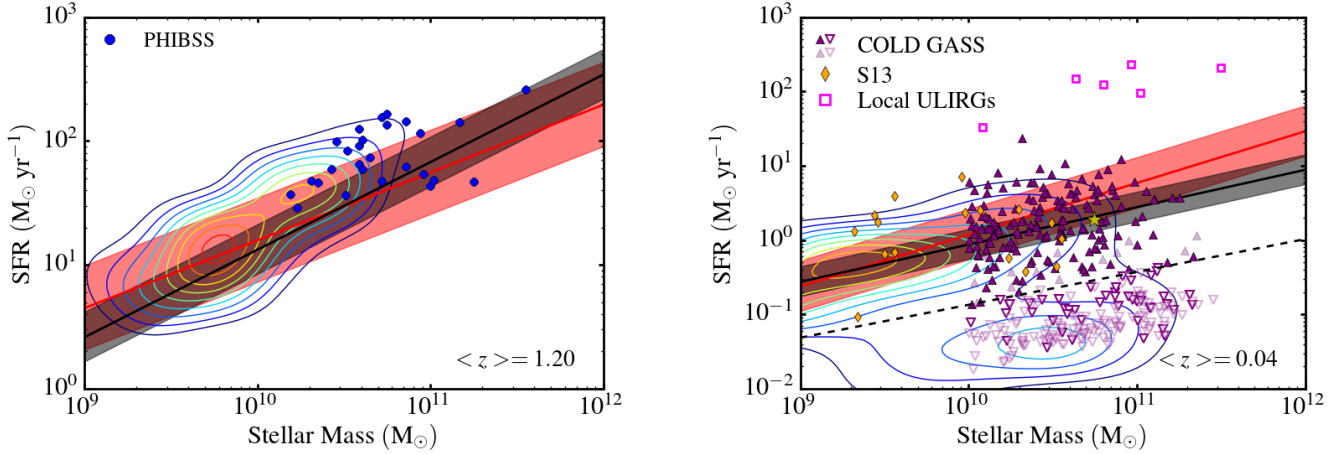


Figure 1. The location of the PHIBSS (*left*) and COLD GASS (*right*) samples in the SFR- M_* plane. Blue points in the left panel correspond to the galaxies in our high- z sample with star formation rates and stellar masses from the RAINBOW database (Barro et al. 2011). Purple triangles in the right panel correspond to galaxies in the low- z sample with stellar masses and star formation rates from the MPA-JHU SDSS catalog. Downward open triangles represent galaxies below our quenching threshold and are not used in the analysis. Shaded points are not detected in CO also not used in the analysis. Additionally shown as orange diamonds are 17 galaxies from Sandstrom et al. (2013) included in the low- z sample. Stellar masses and star formation rates for these galaxies are taken from Kennicutt et al. (2011), with stellar masses derived using H band luminosities and SFRs derived from $H\alpha+24\mu\text{m}$ luminosities. A comparison sample of local ULIRGs, taken from Downes & Solomon (1998), is shown with magenta squares, using stellar masses determined from the H band luminosity (Zibetti, Charlot & Rix 2009) and SFRs calculated from the total infrared luminosity (Kennicutt & Evans 2012). The location of the Milky Way in this space is shown as the yellow star. The dashed line in the right panel indicates the threshold used to separate quenched and star-forming systems in our analysis, as defined in equation 2. For comparison, the black and red lines illustrate fits to the star-forming “main sequence” at $z \sim 0.04$ and $z \sim 1.2$ from Speagle et al. (2014) and Whitaker et al. (2012), respectively, with the black and red shaded regions corresponding to the associated 1σ scatter. To highlight observational scatter, contours of star-forming galaxies from publicly available catalogs are included. In the left panel, contours show galaxies from the RAINBOW database between $1 < z < 1.5$ with spectroscopic redshifts and stellar masses greater than $10^9 M_\odot$, with contours every 75 galaxies per square dex starting at 150 galaxies per square dex. In the right panel, contours show galaxies taken from MPA-JHU catalog with $0.025 < z < 0.05$ and stellar masses greater than $10^9 M_\odot$, with contours every 3,000 galaxies per square dex. Both of our samples draw from typical star-forming galaxies, as 56 per cent of the galaxies in the high- z sample and 42 per cent of galaxies in the low- z sample fall within 0.34 dex of the main sequence from Speagle et al. (2014).

of gas fraction with an approximately uniform star-formation efficiency (assuming a Milky Way α_{CO} , the star-formation efficiency of our COLD GASS sample has a scatter of 0.34 dex, consistent with the intrinsic scatter observed in local galaxies Leroy et al. 2013). Finally, as with PHIBSS, the COLD GASS sample is selected independent of galaxy size or morphology, yielding a representative sampling of the molecular gas in star-forming galaxies at $z \sim 0$.

We combine the sample of integrated CO measurements from COLD GASS with spatially-resolved measurements of α_{CO} for 17 local galaxies as published by Sandstrom et al. (2013). By minimizing the scatter in the dust-to-gas ratio across $\sim\text{kpc}$ -sized regions within nearby ($d < 25$ Mpc) galaxies, Sandstrom et al. (2013) simultaneously determine α_{CO} and the dust-to-gas ratio, mapping their variation within each galaxy. The sample is selected from the *Spitzer* Infrared Nearby Galaxies Survey (SINGS; Kennicutt et al. 2003) and the Key Insights into Nearby Galaxies: A Far-Infrared Survey with *Herschel* (KINGFISH; Kennicutt et al. 2011) programs, with follow-up 21 cm observations as part of The HI Nearby Galaxies Survey (THINGS; Walter et al. 2008) and CO $J=(2 \rightarrow 1)$ observations from the HERA CO Line Emission Survey (HERACLES; Leroy et al. 2009). Of the 26 galaxies analyzed in Sandstrom et al. (2013), the 9 with inclination angles greater than 65° are excluded due to projection effects that complicate the localization of the gas and dust emission. This sample has a median stellar mass slightly less than that of the COLD GASS and PHIBSS samples ($\langle M_* \rangle = 10^{9.8} M_\odot$), but represents the same population of

main-sequence galaxies as the rest of our low- z sample, as shown in Figure 1.

Finally, our low- z sample contains 10 local ULIRGs with existing α_{CO} measurements from the literature. Papadopoulos et al. (2012a), using observations of multiple CO and HCN transitions as constraints on large velocity gradient modeling, determine α_{CO} for a sample of 70 local ULIRGs. The 10 ULIRGs with independent dynamical masses measured by Downes & Solomon (1998) are included in our low- z sample. These ULIRGs tend to be more massive and more intensely star-forming than the rest of our low- z sample (see Fig. 1b), and provide a useful contrast to the more typical galaxies in the Sandstrom et al. (2013) and COLD GASS samples.

2.3 Galaxy Properties

For our high- z sample, we employ the derived galaxy properties from Tacconi et al. (2013), including $^{12}\text{CO } J=(3 \rightarrow 2)$ luminosities, star formation rates, stellar masses, and half-light radii. For the COLD GASS sample, we utilize $^{12}\text{CO } J=(1 \rightarrow 0)$ luminosities from Saintonge et al. (2011a), along with star formation rates and stellar masses from the MPA-JHU catalog of derived galaxies properties for SDSS DR7 (Brinchmann et al. 2004; Kauffmann et al. 2003),³ and u - and r -band Petrosian half-light radii (PetroR50_u, PetroR50_r) from the Sloan Digital Sky Survey Data Release 12

³ <http://wwwmpa.mpa-garching.mpg.de/SDSS/DR7/>

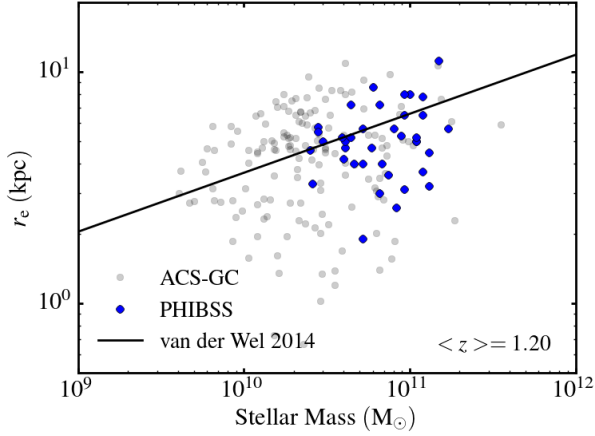


Figure 2. The size-stellar mass distribution for the PHIBSS sample at $z \sim 1.2$ (blue circles). Here, we utilize the I -band (i.e. rest-frame B -band) size for each system, but find similar results when employing $H\alpha$ or rest-frame V - or I -band sizes (see Section 2.4.2). For comparison, gray points show the distribution of star-forming galaxies at $1 < z < 1.5$, utilizing stellar masses from Barro et al. (2011) and I -band sizes from the ACS-General Catalog (Griffith et al. 2012). In addition, the best fit size-mass relation for star-forming galaxies at $z \sim 1$ from van der Wel et al. (2014) is shown as the black line. The PHIBSS sample is not biased towards compact systems; instead, it is consistent with being drawn from the parent population of massive star-forming galaxies at intermediate redshift.

(Alam et al. 2015). In this section, we briefly describe the measurement of these and other galaxy properties for the low- z and high- z samples.

2.3.1 CO Luminosity (L'_{CO})

For the PHIBSS galaxies, CO data cubes obtained with the IRAM Plateau de Bure Millimeter Interferometer (PdBI) map the CO $J=(3 \rightarrow 2)$ line at $\lambda_{\text{rest}} = 0.87$ mm. The CO spectra, obtained from observations of the source in the most compact configuration, are fit to single-component gaussians and integrated along the line of sight to yield the CO flux (F_{CO}). This is converted to a CO $J=(1 \rightarrow 0)$ luminosity using a constant L'_{32}/L'_{10} ratio of 0.5, as suggested by CO ladder observations of high- z star-forming galaxies (Bauermeister et al. 2013b; Daddi et al. 2015; Bolatto et al. 2015).

In the COLD GASS sample, each galaxy is targeted with a single pointing of the IRAM 30-m telescope to observe the CO $J=(1 \rightarrow 0)$ line at $\lambda_{\text{rest}} = 2.6$ mm (Saintonge et al. 2011a). For targets larger than the 22 arcsec beam, aperture corrections are applied by scaling the total flux by the z -band radius measured from the SDSS photometry; however, because COLD GASS galaxies are selected to be at $z > 0.025$, only a small number of systems require this correction. The aperture-corrected CO flux is then integrated along the velocity width of the line and converted to a CO luminosity.

2.3.2 Stellar Masses, Star Formation Rates, and Effective Radii

Stellar masses in both the high- z and low- z samples are determined by fitting template spectral energy distributions (SEDs) to observed photometry. For the high- z sample, the SEDs are fit to 26-band AEGIS photometry, yielding a typical uncertainty of about

0.13 dex. For the low- z sample, the SEDs are fit to SDSS *ugriz*-band photometry corrected for emission-line contributions, yielding a typical uncertainty of approximately 0.1 dex. Further details regarding the SED fitting can be found in Tacconi et al. (2013) and Kauffmann et al. (2003).

Following Wuyts et al. (2011), star formation rates in the high- z sample are calculated according to the calibrated relation from Kennicutt (1998):

$$\text{SFR} = 1.087 \times 10^{-10} [L_{\text{IR}} + 3.3 \nu L_{\nu}(2800\text{\AA})] M_{\odot} \text{ yr}^{-1}, \quad (3)$$

which accounts for both unobscured and obscured star formation as traced by the observed UV and IR luminosities, respectively. The rest-frame UV luminosity is calculated from the best-fit SED, which is primarily constrained by CFHT g' - and i' -band photometric observations that sample rest-frame 2800Å at $z \sim 1 - 1.5$. The total infrared luminosity, tracing obscured star formation and representing $\sim 80\%$ of the total star-forming activity, is calculated from a single far-IR SED extrapolated from the *Spitzer* MIPS 24μm emission. This extrapolation is supported by *Herschel* PACS observations of star-forming galaxies from $z = 0 - 2.5$ (Elbaz et al. 2011), and is sensible for all but the most extreme star-forming systems. Star formation rates for the COLD GASS sample are determined from emission-line luminosities, corrected for aperture losses based on SED fits to *ugriz* photometry. Further details regarding the SFR measurements can be found in Brinchmann et al. (2004).

We use effective radii (r_e) from Tacconi et al. (2013) and the SDSS DR12 (Alam et al. 2015) as size measurements for our high- z and low- z samples, respectively. Unless otherwise stated, in our high- z sample, effective radii are derived from a single component Sérsic fit (Sérsic 1968):

$$I(r) \propto \exp\left[\left(\frac{r}{r_e}\right)^{1/n} - 1\right] \quad (4)$$

to single-orbit *HST*/ACS F814W (rest-frame B -band) images.

As illustrated in Fig. 2, the resulting effective radii in the high- z sample are representative of the star-forming population at this redshift. Moreover, the rest-frame B -band sizes are consistent with the measured extent of the $H\alpha$ emission, as shown in Section 2.4.2. While F606W (rest-frame NUV) imaging is available for only 23 of our high- z objects, our results are qualitatively unchanged when using sizes derived from *HST*/ACS F606W (versus F814W) imaging. For the low- z sample, we utilize the Petrosian half-light radius (PetroR50_u and PetroR50_r) as measured from the SDSS u - and r -band imaging.

2.4 HST/WFC3-IR Grism Observations

A subset (28) of the galaxies in our high- z sample were observed with the *HST*/WFC3-IR G141 grism as part of a Cycle 19 GO program (PID 12547, PI: Cooper) or as part of the 3D-HST program (PID 12177, PI: van Dokkum; Brammer et al. 2012; van Dokkum et al. 2013). The spectral range of the G141 grism extends from 1.1μm to 1.65μm, which traces $H\alpha$ emission at $0.7 \lesssim z \lesssim 1.5$. Both the GO and 3D-HST observations are two orbits deep, corresponding to an approximate 5σ $H\alpha$ detection limit of $\sim 5 \times 10^{-17} \text{ erg s}^{-1} \text{ cm}^{-2}$. Accompanying direct image exposures provide the necessary information for source identification and contamination corrections. The WFC3-IR images were processed utilizing the CALWF3 reduction pipeline, with the grism spectra and corresponding contamination images extracted using the AXE reduction pipeline (Kümmel et al. 2009; Weiner et al. in prep). All but three (i.e. 25 out of the 28) galaxies are detected in $H\alpha$ emission

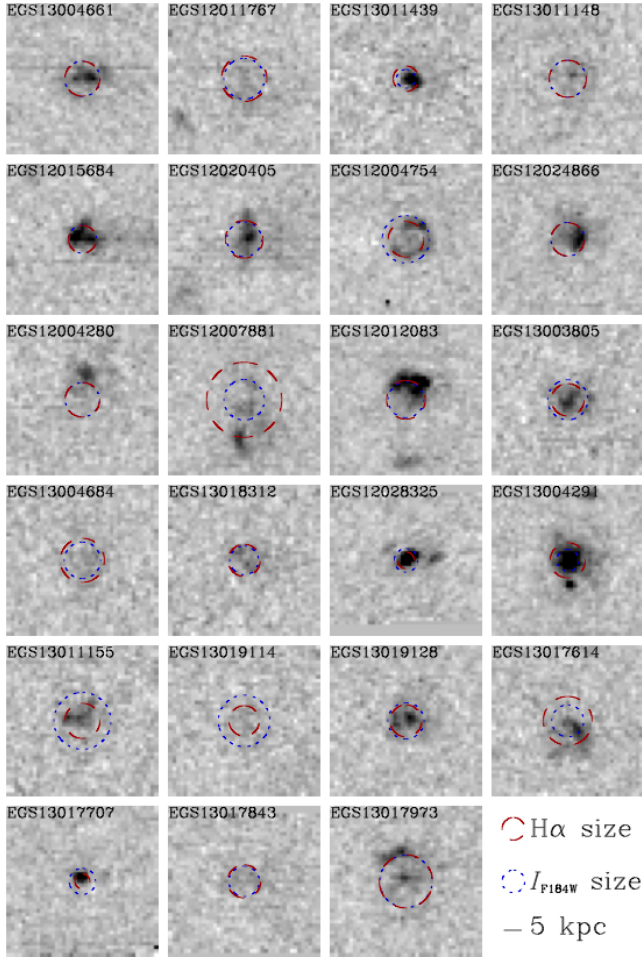


Figure 3. $H\alpha$ images derived from *HST*/WFC3-IR G141 grism observations for a subset of our PHIBSS sample at $z \sim 1$. For each galaxy, the measured $H\alpha$ size and *HST*/ACS I -band size are illustrated by the dashed red circle and dot-dashed blue circle, respectively. In general, the $H\alpha$ and broad-band sizes are in very good agreement, with an average difference of less than 0.1 physical kpc. As a reference, the legend includes a bar corresponding to 5 kpc (physical) at the redshift of our high- z sample ($z = 1.2$).

at the 5σ level; we exclude an additional two systems for which the $H\alpha$ emission is located too close to the edge of the WFC3-IR detector.

2.4.1 $H\alpha$ SFR

The $H\alpha$ emission probed by the *HST*/WFC3 grism observations provides a valuable cross-check of the SFR measurements inferred from broad-band photometry. The advantage of using $H\alpha$ emission as an independent SFR indicator is two-fold. First, $H\alpha$ emission from HII regions around young (< 10 Myr old) stars provides a more instantaneous star-formation indicator than UV and IR broad-band emission. Second, SFR measurements from $H\alpha$ are free from the assumptions and uncertainties of SED fitting techniques. We calculate the star formation rate ($SFR_{H\alpha}$) from the observed $H\alpha$ luminosity ($L_{H\alpha}$) according to the empirical relation of Kennicutt & Evans (2012) adjusted to a Chabrier IMF following Twite et al. (2012):

$$SFR_{H\alpha} = 4.6 \times 10^{-42} L_{H\alpha} \times 10^{0.4A_{H\alpha}}, \quad (5)$$

where the $H\alpha$ luminosity is determined by integrating the $H\alpha$ emission from the continuum subtracted one-dimensional grism spectrum. Continuum emission is fit to a third-order polynomial, with a $\sim 400\text{\AA}$ region around the emission line masked from the fit.

To correct for contamination from nearby [NII] $\lambda\lambda 6548, 6583$ emission, we use the strong correlation between the [NII]– $H\alpha$ ratio and gas-phase metallicity (Pettini & Pagel 2004). The metallicity of each system is inferred from the measured stellar mass according to the mass-metallicity relation of Zahid et al. (2014) and then converted to the [NII]/ $H\alpha$ -based metallicity scale of Pettini & Pagel (2004) using the conversion from Kewley & Ellison (2008):

$$12 + \log O/H = 8.90 + 0.57 \times [NII]/H\alpha. \quad (6)$$

The NII emission (typically 30 per cent of the observed emission line) is then subtracted from the integrated luminosity to determine the $H\alpha$ luminosity. We estimate the relevant extinction ($A_{H\alpha}$) from the observed infrared excess (IRX):

$$A_{H\alpha} = 1.37 \log[1 + 3.89 L_{24\mu m}/L_{FUV}], \quad (7)$$

where $IRX = \log[L(TIR)/L(FUV)]_{obs}$ (Hao et al. 2011). To calculate the IRX, we use a combination of rest-frame $24\mu m$ and FUV synthetic photometry from SED fits available in the RAINBOW database.

The resulting $H\alpha$ star formation rates agree with the corresponding UV+IR star formation rates from Tacconi et al. (2013), with the $H\alpha$ SFRs only 0.03 dex lower on average. The scatter between the $H\alpha$ and UV+IR star formation rates, however, is large, with an rms difference of 0.49 dex. While some of this scatter can be attributed to the uncertainty in the [NII] subtraction (~ 0.1 dex) and intrinsic scatter in the IRX-based $A_{H\alpha}$ estimates (~ 0.13 dex), the large scatter is likely due to 73 per cent of the sample having an $H\alpha$ extinction greater than 2.5 mag, beyond the calibration of Hao et al. (2011). As a result, we employ the UV+IR star formation rates for the remainder of the analysis, though our results are qualitatively unchanged if we use the $H\alpha$ star formation rates.

2.4.2 $H\alpha$ Size

It is known that galaxy sizes vary with rest-frame color, with red images tracing the more concentrated stellar component and blue images tracing the extended star-forming component (Nelson et al. 2012; van der Wel et al. 2014). In light of this, we test whether the I -band radii are an accurate indicator of the size of the star-forming component in the $z \sim 1$ galaxies by measuring effective radii from the grism $H\alpha$ images. Because of its low spectral resolution, the *HST*/WFC3-IR G141 grism spectra can be thought of as a sequence of adjacent images, taken at 101\AA increments, such that any observed structure along the spectral direction must be spatially extended as outflows would need a radial velocity of $V > 2000 \text{ km s}^{-1}$ to yield a resolved Doppler shift. For each row in the grism image, we mask the $H\alpha$ emission and fit a third-order polynomial to the continuum, using the same procedure as outlined in Section 2.4.1. This continuum is then subtracted from the contamination-subtracted grism image to generate maps of the $H\alpha$ emission (see Fig. 3). The advantage of the grism is apparent; spatial structure that would have been missed by a high-resolution spectroscopic observation is readily apparent.

Due to strong asymmetry and clumpiness in the $H\alpha$ emission, measuring a size (i.e. r_e) via a parametric fit to the light profile is often problematic. Instead, we measure r_e by constructing curves of growth from the $H\alpha$ images. The curves of growth are centered on the wavelength of $H\alpha$ in the spectral direction (as determined from

the DEEP2/DEEP3 spectroscopic redshift) and the center of the continuum in the spatial direction, which is taken to be the median centroid of Gaussian fits to each column of continuum emission. Rather than using a fixed aperture to determine the total enclosed flux, we utilize the first aperture, for which the curve of growth decreases in two subsequent apertures (spaced at radial increments of $0.13''$). The radius at which the curve of growth passes half of this total flux is identified as the effective radius.

As illustrated in Figure 3, the measured $\text{H}\alpha$ sizes agree with those derived from the *HST*/ACS *I*-band imaging; the median absolute difference between the two sizes ($|r_{\text{H}\alpha} - r_I|$) is 0.07 kpc with an rms scatter of 1.6 kpc. While individual galaxies may deviate by greater than the statistical uncertainty of the size measurement (typical uncertainty is 0.14 kpc or roughly 3 per cent), they are within the systematic uncertainty associated with non-uniform extinction and ellipticity. The agreement in size measurements is consistent with both the $\text{H}\alpha$ and UV emission being dominated by star formation. Nelson et al. (2012) employ a similar procedure to compare $\text{H}\alpha$ sizes of $z \sim 1$ galaxies on the main sequence with rest-frame *R*-band sizes and find that $\text{H}\alpha$ emission tends to be more extended than *R*-band emission in star-forming galaxies, especially for the most extended ($r_e > 5$ kpc *R*-band) systems. Although 9 galaxies in our high- z sample with grism observations have sizes greater than 5 kpc, we do not see strong evidence of this bias. This is likely because the *I*-band measurements are blueward of the rest-frame 4000Å break for most of our high- z sample and primarily trace the star-forming component. Among systems with H_{F160W} observations, our results are consistent with those of Nelson et al. (2012), with $\text{H}\alpha$ sizes 17% larger than H_{F160W} (rest frame *R* band) sizes on average. As we have no evidence for bias in the *I*-band size measurement, and the *I*-band ACS images have higher spatial resolution, we use the *I*-band sizes throughout the remainder of our analysis.

3 ESTIMATING THE CO- H_2 CONVERSION FACTOR

In order to constrain α_{CO} , we require an independent measurement of the molecular gas mass – i.e. one not derived from the observed CO line flux. Often, studies of α_{CO} utilize H_2 masses inferred from the dynamics of resolved gas clouds (Ade et al. 2011), other cold molecular gas tracers (e.g. ^{13}CO , Papadopoulos et al. 2012a), or cold dust emission coincident with molecular gas (Leroy et al. 2011; Sandstrom et al. 2013). For our samples, however, we lack the sensitive complementary observations necessary for these traditional techniques.⁴

While we are unable to apply these conventional methods to measure M_{gas} , we can indirectly probe the molecular gas reservoir via the observed star formation rate, assuming a particular relationship between the current star-forming activity and the total molecular gas mass (e.g. Genzel et al. 2012). This relationship is quantified in terms of the molecular gas depletion time, $t_{\text{dep}} = M_{\text{gas}}/\text{SFR}$, which is shown to be largely independent of atomic and molecular gas fractions at $z \sim 0$ (Bigiel et al. 2008, 2011). Furthermore, millimeter observations of molecular gas in local main-sequence galaxies measure an approximately constant depletion time on kpc-scales, mostly independent of gas surface density and indicative of

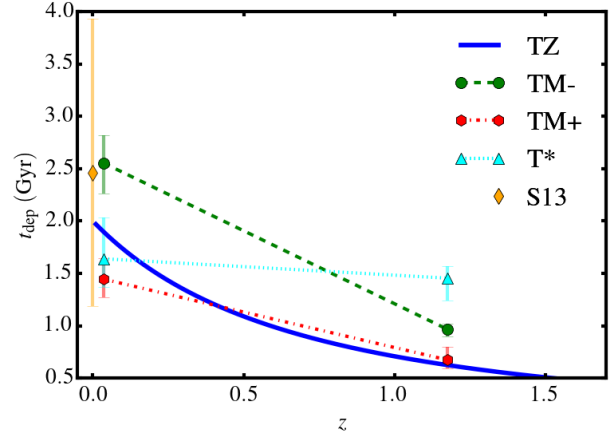


Figure 4. A summary of the depletion time models adopted in our calculation of α_{CO} . As model TZ is solely dependent on z , it is shown as a solid line from $z \sim 0$ to $z \sim 1$. For models TM-, TM+, and T*, points represent the median depletion time value within the COLD GASS and PHIBSS samples and error bars correspond to the 33 – 66 percentile range of the corresponding t_{dep} distribution. For context, the orange point illustrates the median, CO-independent, t_{dep} measurement within the Sandstrom et al. (2013) sample, with error bars again corresponding to the 33 – 66 percentile range of the distribution. The difference in the assumed dependence of t_{dep} on z and stellar mass across the four models allows us to probe potential systematic uncertainties associated with the relationship between α_{CO} and total mass surface density (or metallicity). Although models TM-, TM+, and T* are all normalized to 2 Gyr at a stellar mass of $10^{10.7} M_{\odot}$ at $z = 0$, the different stellar mass dependencies of the models result in different median depletion times in the low- z sample.

a homogeneous star-formation process (Bigiel et al. 2011; Leroy et al. 2013; Huang & Kauffmann 2014).

Assuming a universal depletion timescale, we can determine the molecular gas mass from a galaxy’s star formation rate, leading us to an expression for α_{CO} :

$$\alpha_{\text{CO}} = \frac{\text{SFR } t_{\text{dep}}}{L'_{\text{CO}}}. \quad (8)$$

At present, there is considerable uncertainty regarding the dependence of t_{dep} on galaxy properties and cosmic time. However, observations of nearby galaxies find evidence for variation in t_{dep} with stellar mass (Saintonge et al. 2011b; Leroy et al. 2013; Boselli et al. 2014) and specific star-formation rate (Saintonge et al. 2011b, 2012; Boselli et al. 2014; Genzel et al. 2015). In addition, reduced depletion times have been observed within dense galaxy centers (Leroy et al. 2013), and trends between t_{dep} and gas density (Kennicutt 1998; Kennicutt & Evans 2012; Genzel et al. 2010), stellar surface density (Boselli et al. 2014), and the dynamical time of the gas (Kennicutt 1998; Kennicutt et al. 2007) have been observed. To ensure that any observed relationships between α_{CO} and galaxy properties within our samples are not simply artifacts of an underlying correlation with depletion time, we use four physically-motivated models for t_{dep} , covering a range of possible relationships between t_{dep} and galaxy properties⁵ and/or redshift. The de-

⁴ Upcoming observations as part of PHIBSS2 (Tacconi et al. in prep) will resolve CO emission within a sample of galaxies at $z \sim 1$, providing additional constraints on our measurements.

⁵ We do not include a density-dependent depletion time model in our primary analysis, but our results remain qualitatively unchanged when a density-dependent t_{dep} law is adopted (see Section 5.4).

pletion time models we employ are:

$$t_{\text{dep}} \text{ (Gyr)} = 2 \times (1+z)^{-1.5}, \quad (\text{TZ})$$

$$t_{\text{dep}} \text{ (Gyr)} = 2 \times (1+z)^{-1.5} \left(\frac{M_*}{10^{10.7} \text{ M}_\odot} \right)^{0.36}, \quad (\text{TM+})$$

$$t_{\text{dep}} \text{ (Gyr)} = 2 \times \left(\frac{t_H}{13.5 \text{ Gyr}} \right) \left(\frac{M_*}{10^{10.7} \text{ M}_\odot} \right)^{-0.3}, \quad (\text{TM-})$$

$$t_{\text{dep}} \text{ (Gyr)} = 2 \times \left(\frac{\text{sSFR}}{\langle \text{sSFR} \rangle_z} \right)^{-0.44}, \quad (\text{T*})$$

where M_* and sSFR are the stellar mass and specific star formation rate of the system, t_H is the Hubble time at the appropriate redshift, and $\langle \text{sSFR} \rangle_z$ is a redshift-dependent normalization parameter.

Model TZ, which is independent of galaxy properties and smoothly decreasing with increasing redshift, represents the simplest of our assumed t_{dep} models. The normalization is set by COLD GASS observations at $z \sim 0.1$ (Saintonge et al. 2011b), while the redshift dependence, which is slightly steeper than that derived in Tacconi et al. (2013) or Genzel et al. (2015), traces the evolution of the dynamical time and reproduces complementary observations at higher z (Bauermeister et al. 2013a; Geach et al. 2011; Saintonge et al. 2013; Magdis et al. 2012b). The positive correlation between t_{dep} and M_* in model TM+ is taken from the Saintonge et al. (2011b) fit to COLD GASS observations, and is interpreted as the consequence of bulge growth stabilizing gas in the disk and suppressing star formation (e.g. Martig et al. 2009).

The mass and redshift dependence in model TM- matches the prescription of Davé, Finlator & Oppenheimer (2012), found by associating the depletion time with the local dynamical time.⁶ This model is normalized such that galaxies at $z = 0$ with a stellar mass of $10^{10.7} \text{ M}_\odot$ have a 2 Gyr depletion time, consistent with models TZ and TM+. Finally, model T* replicates the measured dependence of t_{dep} on sSFR as observed by Saintonge et al. (2011b), normalized to 2 Gyr at a sSFR of $10^{-10.4} \text{ yr}^{-1}$ for the low- z sample and $10^{-9.2} \text{ yr}^{-1}$ for the high- z sample.⁷ This sSFR dependence is consistent with the findings of Genzel et al. (2015), who, using a broad range of CO- and dust-based molecular gas measurements, report $t_{\text{dep}} \propto (\text{sSFR}/\text{sSFR}_{\text{MS}})^{-0.49}$, where sSFR_{MS} is the sSFR of a galaxy on the main sequence at a given stellar mass and redshift (see also Tacconi et al., in prep). This model attempts to incorporate variation in star-formation efficiency that may drive the scatter in the star-forming main sequence. Galaxies with lower depletion times necessarily have a higher sSFR, as they are able to convert their molecular gas reservoir into star formation more efficiently.

Figure 4 illustrates the median redshift dependence (and scatter) of t_{dep} values for each model as applied to the COLD GASS and PHIBSS samples. For our four models, the evolution in the resulting depletion times, as well as their scatter at fixed z , varies significantly. The difference in assumed dependence on z and stellar mass, in particular, allows us to probe potential systematic uncertainties associated with the relationship between α_{CO} and total mass surface density. Model TM- yields the strongest evolution in t_{dep} due,

in large part, to the difference in median stellar mass between our low- z and high- z samples and the assumed mass dependence of that model. Altogether, it is important to note that our approach for estimating α_{CO} will not be accurate on an object-by-object basis. The inferred α_{CO} estimates are meaningful on average, however, allowing us to explore – in a statistical sense – the global trends of α_{CO} with galaxy properties and/or redshift.

4 DEPENDENCE OF α_{CO} ON Σ_{tot}

The expected relationship between α_{CO} and total (baryonic) mass surface density (Σ_{tot}) in our sample depends on the primary phase of molecular gas within the systems. The α_{CO} value of GMCs in the Milky Way disk is largely insensitive to the surrounding galactic environment, with no significant evidence for a correlation between α_{CO} and Σ_{tot} (Solomon et al. 1987; Ade et al. 2011). A correlation between α_{CO} and Σ_{tot} has been observed, however, within ‘diffuse’ clouds of molecular gas (Downes & Solomon 1998; Sandstrom et al. 2013). For example, at the centers of local ULIRGs, observations indicate that molecular gas primarily exists as an extended molecular cloud (100s of pc in diameter) containing stars, individual molecular clouds, and diffuse molecular gas (Downes & Solomon 1998; Leroy et al. 2015). This diffuse gas has a higher velocity dispersion (and thus lower α_{CO}) than a similarly massive, but isolated cloud due to the contribution of enclosed stars to the gravitational potential. For such a cloud, the dependence of α_{CO} on total mass surface density roughly follows the relation: $\alpha_{\text{CO}} \propto \Sigma_{\text{tot}}^{-0.5}$ (Bolatto, Wolfe & Leroy 2013), reflecting the dependence of the velocity dispersion (i.e. L'_{CO}) on total mass surface density (Downes & Solomon 1998). This description is consistent with observations of local ULIRGs (Papadopoulos et al. 2012a), simulations of molecular gas in disks and mergers (Narayanan et al. 2011), as well as (on a smaller scale) the lower α_{CO} values observed at the centers of local star-forming systems (Sandstrom et al. 2013).

While this correlation between α_{CO} and Σ_{tot} is only expected to lower α_{CO} in a diffuse molecular cloud within a high-density region of a galaxy, it may dictate the galaxy-wide α_{CO} value if a significant fraction of the total molecular gas is in this phase. To first order, the galaxy-integrated α_{CO} can be thought of as the mass-weighted average of α_{CO} in diffuse cloud(s) (α_D) and in the rest of the galaxy (α_G), assumed to be composed of self-gravitating GMCs:

$$\langle \alpha_{\text{CO}} \rangle = \frac{\alpha_D \alpha_G}{f_d \alpha_G + (1 - f_d) \alpha_D}, \quad (9)$$

where f_d is the (mass) fraction of molecular gas in the diffuse phase. Observations of both low- and high- z ULIRGs point to galaxy-wide α_{CO} values close to $0.8 \text{ M}_\odot (\text{K km s}^{-1} \text{ pc}^2)^{-1}$ (Downes & Solomon 1998; Papadopoulos et al. 2012b; Magdis et al. 2011; Spilker et al. 2015), consistent with the decrease in α_{CO} expected for a galaxy with a large fraction of its gas in a diffuse phase. On the other hand, the average α_{CO} value for molecular gas in local star-forming galaxies largely mirrors the Milky Way value (Sandstrom et al. 2013), consistent with gas that primarily resides in self-gravitating GMCs.

By investigating the relationship between α_{CO} and total mass surface density for a large sample of galaxies at $z \sim 0$ and $z \sim 1$, our study probes the evolution of molecular gas conditions over cosmic time. In particular, we investigate the possibility that the structure of molecular gas at $z \sim 1$ is significantly different from that observed at $z \sim 0$, with more gas in large (kpc-scale) star-forming

⁶ Davé, Finlator & Oppenheimer (2012) do not distinguish between atomic and molecular gas; however, the molecular component is expected to be dominant with our sample, such that the inclusion or exclusion of atomic gas should not significantly affect our results.

⁷ The redshift dependence of this normalization is chosen to match the global sSFR evolution from Pérez-González et al. (2008)

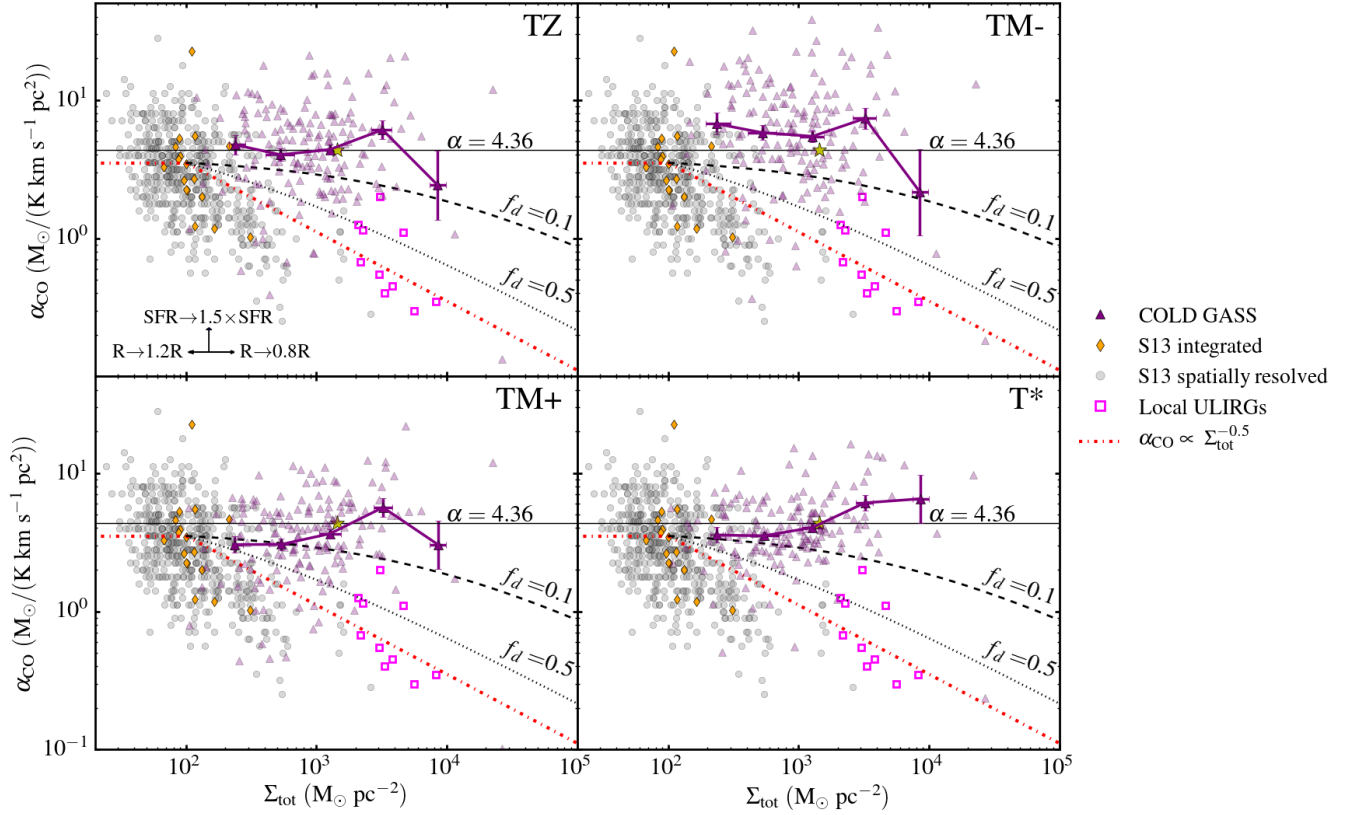


Figure 5. The dependence of α_{CO} on total mass surface density (Σ_{tot}) in the low- z sample. The four panels, as labeled, correspond to α_{CO} values inferred via each of our assumed t_{dep} models. Across all panels, grey points show spatially-resolved, dust-based measurements of α_{CO} in local galaxies from Sandstrom et al. (2013), exhibiting both regions diffuse (high Σ_{tot} and low α_{CO}) and self-gravitating (Milky Way α_{CO}) gas, with orange diamonds representing the galaxy-averaged values. Additionally, magenta points correspond to measurements of local ULIRGs, with Σ_{tot} from Downes & Solomon (1998) and α_{CO} based on single component fits from Papadopoulos et al. (2012a). The faint purple triangles show our measurements for the 164 star-forming galaxies in our low- z sample from COLD GASS, with the dark purple points illustrating the mean α_{CO} for this sample across 5 distinct bins in Σ_{tot} ranging from $125 \text{ M}_{\odot} \text{ pc}^{-2} < \Sigma_{\text{tot}} < 1.6 \times 10^4 \text{ M}_{\odot} \text{ pc}^{-2}$. For the binned measurements, the horizontal error bar indicates the 25 – 75% range in Σ_{tot} for the population within the given bin, and the vertical error bar shows the 1σ error on the mean α_{CO} value. Vectors in the lower-left corner of the top-left panel indicate how a change in SFR or r_e affect our measurements of α_{CO} and Σ_{tot} . The red, dot-dashed line indicates the relationship between α_{CO} and Σ_{tot} for molecular gas within galaxies, as suggested by Bolatto, Wolfire & Leroy (2013), Eq. 31, shifted to the average metallicity of our low- z sample according to the mass-metallicity relation of Zahid et al. (2014). The dotted and dashed black lines denote models for the dependence of α_{CO} on surface density assuming a mix of diffuse molecular gas (with $\alpha_{\text{CO}} \propto \Sigma_{\text{tot}}^{-0.5}$) and gas in Milky Way-like GMCs (with a constant α_{CO} ; see equation 9). The dotted line represents a 50 – 50 mix, by mass, of diffuse gas and GMC-like gas, and the dashed line represents a mix of 10% diffuse gas and 90% GMC-like gas. The α_{CO} points within the COLD GASS sample do not show a significant decrease with increasing total mass surface density, consistent with a population that contains a small fraction molecular gas in diffuse, extended clouds.

clumps than self-gravitating GMCs, as suggested by high- z IFU observations (Förster Schreiber et al. 2009; Genzel et al. 2011; Ceverino, Dekel & Bournaud 2010). In this case (high f_d), the stellar mass enclosed in these clouds would raise their velocity dispersion, leading to a negative correlation between α_{CO} and Σ_{tot} at $z \sim 1$. However, if most of the gas is in the form of GMCs similar to those in the Milky Way disk (low f_d), we expect a constant α_{CO} , independent of Σ_{tot} .

4.1 COLD GASS

Figure 5 shows the relationship between α_{CO} and total mass surface density in our low- z sample. Throughout, we define total mass surface density as the total stellar and gas mass for each system divided by the area within r_e :

$$\Sigma_{\text{tot}} = \frac{M_* + M_{\text{H}_2} + M_{\text{HI}}}{\pi r_e^2}. \quad (10)$$

When calculating Σ_{tot} , M_{H_2} is inferred from the associated t_{dep} model, in order to be consistent with the rest of the analysis. In our low- z sample, stellar mass represents the dominant mass component, with $M_{\text{gas}}/(M_{\text{gas}} + M_*) \sim 22\%$ on average, such that we adopt the r -band Petrosian half-light radius for r_e . Our results remain unchanged, however, when taking r_e to be the u -band Petrosian half-light radius, which tracks the typically more-extended light associated with star formation. Alongside the COLD GASS sample in Fig. 5, we also plot α_{CO} values determined from fits to molecular emission in local ULIRGs, assuming a single component ISM model, from Papadopoulos et al. (2012a) and dust-based α_{CO} measurements from Sandstrom et al. (2013), which track α_{CO} in kpc-sized regions in local ULIRGs and disk galaxies, respectively. These measurements from the literature show that gas in the densest regions of galaxies is affected by the galactic environment, such that α_{CO} decreases with increasing Σ_{tot} . In contrast to these spatially-resolved measurements, however, the system-wide

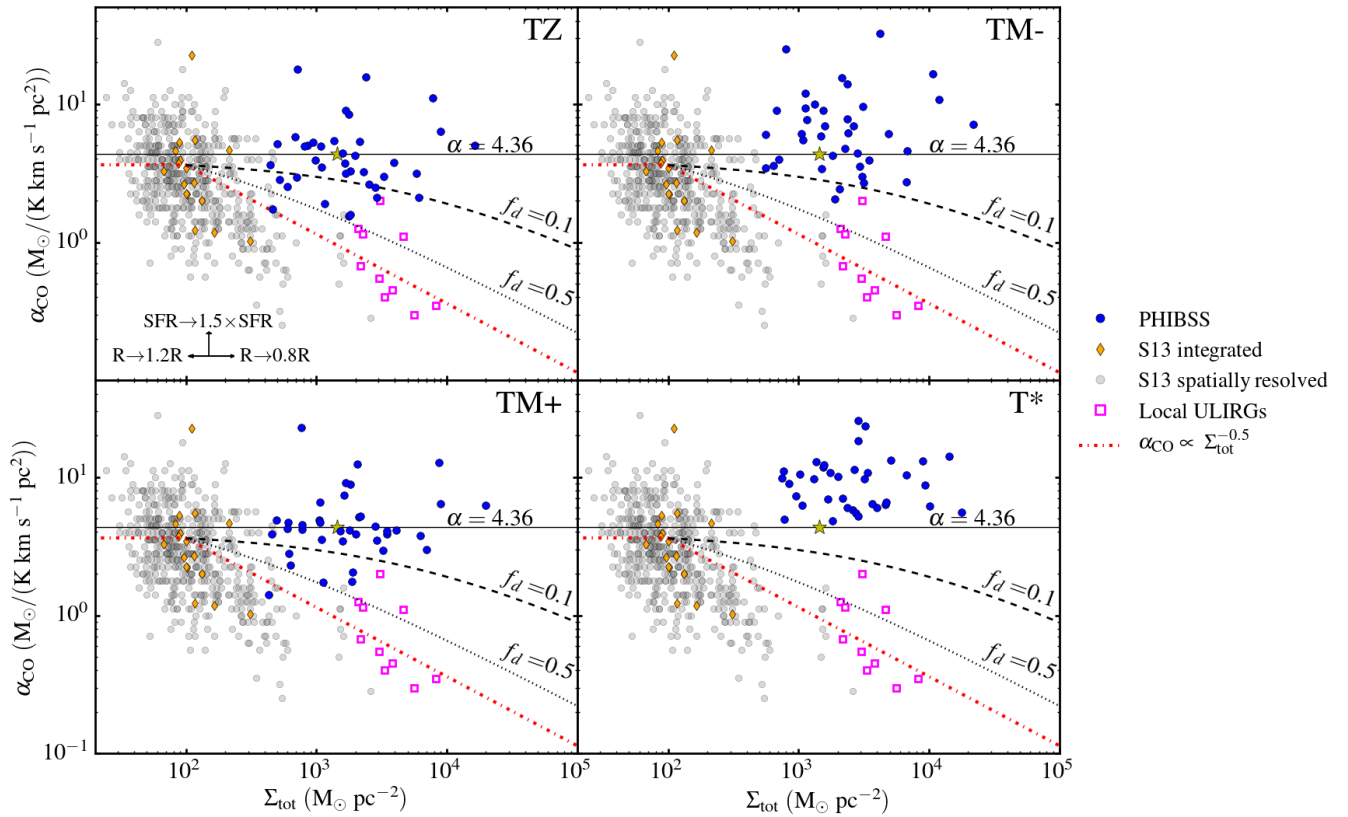


Figure 6. The dependence of α_{CO} on mass surface density for the PHIBSS sample. Blue circles represent our measurements of galaxies in PHIBSS, with the t_{dep} model used in each α_{CO} calculation shown in the top of each panel, whereas grey, orange, and magenta points are the same as in Figure 5. Vectors in the lower-left corner of the top-left panel indicate how a change in SFR or r_e affect our measurements of α_{CO} and Σ_{tot} . Motivated by the noticeable trend between α_{CO} and surface density in the grey and magenta points, some models (Narayanan et al. 2012; Bolatto, Wolfire & Leroy 2013) suggest that α_{CO} decreases smoothly with increasing surface density in extended molecular clouds. As in Figure 5, we show the model from Bolatto, Wolfire & Leroy (2013), Eq. 31, shifted to the metallicity of our high- z sample (following the redshift-dependent mass-metallicity relation of Zahid et al. (2014)) as the red dot-dashed line and include models for the dependence of α_{CO} on surface density assuming a mix of diffuse molecular gas (with $\alpha_{\text{CO}} \propto \Sigma_{\text{tot}}^{-0.5}$) and gas in Milky Way-like GMCs (with a constant α_{CO} ; see Equation 9). The black dotted line represents a 50-50 mix, by mass, of diffuse gas and GMC-like gas, and the black dashed line represents a mix of 10% diffuse gas and 90% GMC-like gas. The α_{CO} points within the PHIBSS sample do not show a significant decrease with increasing surface density, suggesting that molecular gas is primarily in the form of self-gravitating GMCs as opposed to large star-forming clumps.

(or integrated) α_{CO} values for the Sandstrom et al. (2013) sample do not show a correlation between α_{CO} and Σ_{tot} , indicative of a molecular gas component dominated by Milky Way-like GMCs. As a connection between our understanding of α_{CO} in individual molecular clouds and galaxy-wide α_{CO} values, Fig. 5 shows the expected trend between α_{CO} and Σ_{tot} with 10% and 50% of gas (by mass, following Equation 9) residing in a diffuse phase (black dashed and dotted lines, respectively) — where we assume $\alpha_G = \alpha_{\text{MW}}$ shifted to the average metallicity of the low- z sample ($2.6 M_{\odot} (\text{K km s}^{-1} \text{pc}^2)^{-1}$ independent of Σ_{tot}), and $\alpha_D \propto \Sigma_{\text{tot}}^{-0.5}$, normalized to $2.6 M_{\odot} (\text{K km s}^{-1} \text{pc}^2)^{-1}$ at $\Sigma_{\text{tot}} = 100 M_{\odot} \text{pc}^{-2}$.

For the COLD GASS sample, which probes total mass surface densities intermediate between that of local ULIRGs and the Sandstrom et al. (2013) sample, we do not find a decrease in α_{CO} with increasing Σ_{tot} . Independent of the depletion time model assumed, the inferred α_{CO} values are not significantly lower for the high-density systems relative to their low-density counterparts. An ordinary least-squares linear regression between α_{CO} and Σ_{tot} reveals that none of the t_{dep} models yield a slope more than 1σ below 0. The lack of a significant trend between α_{CO} and total mass surface density suggests that CO-emitting molecular gas within the

COLD GASS sample is primarily in the form of self-gravitating GMCs similar to those in the Milky Way disk.

4.2 PHIBSS

Figure 6 shows the relationship between α_{CO} and total mass surface density in our high- z sample, where Σ_{tot} is again calculated as the total stellar and (molecular) gas mass divided by the area within r_e . Excluding the atomic gas component in our high- z sample probably does not significantly affect our results, especially recognizing that H I represents $\lesssim 10\%$ of the baryonic content in massive galaxies locally (Catinella et al. 2010). Although it traces bluer, slightly more extended emission than the r -band measurements used in the low- z sample, the I -band size is employed in this calculation due to its high spatial resolution and sensitivity.

As for the low- z sample, we find no significant correlation between α_{CO} and Σ_{tot} : a linear fit to the data shows that none of the assumed t_{dep} models yield α_{CO} values that decrease with increasing surface density. This result remains unchanged when utilizing complementary $H\alpha$, J_{F120W} , or H_{F160W} size measurements to measure Σ_{tot} (see Sec. 5.2 for a discussion of how the distribution of molecular gas in our systems impacts our results). Overall, the relation-

ship between α_{CO} and surface density in the PHIBSS sample is discrepant with a scenario in which molecular gas in high- z galaxies is primarily in the form large, diffuse clouds, like those found in high-density galaxy centers or merger-driven ULIRGs. Model T* points are higher than those of our other models; however, uncertainties in the redshift evolution of t_{dep} result in significant uncertainties in the normalization of our high- z α_{CO} values (see Sec. 5.5). Values of α_{CO} for our T* model are greater than those of our other depletion time models, in part due to differences in the star formation rate indicators used to track the evolution of the sSFR (and thus the redshift-dependent normalization of the T* model) versus that used to measure the SFRs for our high- z sample (note that model T* has the highest average t_{dep} among our models at high- z ; see Fig. 4). An additional redshift dependence in model T*, like that suggested in Genzel et al. (2015, $t_{\text{dep}} \propto (1+z)^{-0.3}$), would lower the model T* α_{CO} values, significantly reducing the discrepancy between the model T* points and the Milky Way value. Regardless, the model T* α_{CO} values are consistent with the non-correlation between α_{CO} and Σ_{tot} observed for the rest of the models.

As in Fig. 5, black dashed and dotted lines in Fig. 6 indicate the predicted correlation between α_{CO} and Σ_{tot} for a sample with 10% and 50% of the molecular gas in a diffuse phase respectively. The PHIBSS data are consistent with $\lesssim 10\%$ of the molecular gas in typical massive star-forming galaxies residing in a diffuse phase (contributing $\lesssim 30\%$ of the CO luminosity), with the vast majority of gas contained within self-gravitating GMCs.

The lack of an observed decrease in α_{CO} for high-density star-forming galaxies at $z \sim 1$ is arguably more surprising than the same result at $z \sim 0.05$. The high- z sample is much more dense on average than the low- z sample ($\langle \Sigma_{\text{tot}} \rangle = 1600 \text{ M}_{\odot} \text{ pc}^{-2}$ for PHIBSS compared with $\langle \Sigma_{\text{tot}} \rangle = 800 \text{ M}_{\odot} \text{ pc}^{-2}$ for COLD GASS) and contains a higher fraction of highly star-forming ULIRGs than the low- z sample, both thought to be indicative of low α_{CO} values. Regardless of the depletion time model adopted, however, most (92 – 100 per-cent) of the α_{CO} measurements are closer to the Milky Way value ($4.36 \text{ M}_{\odot} (\text{K km s}^{-1} \text{ pc}^2)^{-1}$) than the canonical ULIRG value ($0.8 \text{ M}_{\odot} (\text{K km s}^{-1} \text{ pc}^2)^{-1}$). Despite the changing ISM conditions between $z \sim 0$ and $z \sim 1$, the trend between α_{CO} and density in the high- z sample follows the invariance between α_{CO} and surface density observed in the COLD GASS sample locally, which suggests that the molecular gas in typical star-forming galaxies at $z \sim 1$ is primarily in the form of self-gravitating GMCs instead of large, diffuse clouds.

5 DISCUSSION

Across a broad range of assumed molecular depletion times, we do not observe a significant correlation between α_{CO} and total mass surface density for our sample of massive star-forming galaxies at $z \sim 0$ and $z \sim 1$. Instead, our analysis indicates that objects in our sample primarily contain molecular gas in the form of self-gravitating GMCs as opposed to in a diffuse phase. This result is somewhat surprising, particularly at high- z , where observations suggest that kpc-scale clumps contribute substantially ($\sim 20\%$) to the galaxy-wide SFR (Förster Schreiber et al. 2011; Genzel et al. 2011; Wuyts et al. 2012) and potentially form stars in a similar process to that observed in local ULIRGs. Rather, we find that the molecular gas in typical star-forming systems, at both low- and high- z , is primarily in the form of self-gravitating molecular clouds. In this section, we investigate possible systematic effects that could impact our results.

5.1 Temperature and Excitation Effects

If the high-density galaxies in our sample have systematically lower ISM temperatures, the molecular gas would be less luminous despite its elevated dispersion, thereby increasing α_{CO} so as to potentially flatten an existing correlation between α_{CO} and Σ_{tot} . Observations of cold gas in star-forming galaxies with *Herschel*, however, indicate that gas temperatures remain remarkably constant between $z \sim 1$ and $z \sim 0$ in typical systems (Dunne et al. 2011; Elbaz et al. 2010; Magnelli et al. 2014; Béthermin et al. 2015). Moreover, observations of mergers and ULIRGs typically yield gas temperatures elevated by a factor of 2 – 4 (not lower) relative to that measured in normal star-forming systems (Krumholz & Thompson 2007; Papadopoulos et al. 2012b; Kamenetzky et al. 2014). Such elevated gas temperatures would produce lower α_{CO} values, so as to strengthen a potential correlation between α_{CO} and surface density, not weaken it.

Furthermore, given that the brightness temperature ratio $L'_{32}/L'_{10}(r_{31}) = 0.5$ is directly linked to the inferred CO $J=(1 \rightarrow 0)$ luminosity, any systematic variation of r_{31} across our $z \sim 1$ sample would directly influence our α_{CO} observations. Although the excitation temperature is linked with gas density on the scales of individual clouds, global r_{31} values exhibit little variation with integrated galaxy properties. The value of $r_{31} = 0.5$ has been observed in both normal galaxies (Mauersberger et al. 1999; Yao et al. 2003) and local ULIRGs (Papadopoulos et al. 2012a; Bauermeister et al. 2013b; Daddi et al. 2015). While there is significant (40%) scatter in measured r_{31} values, no strong correlation between r_{31} and stellar mass, star formation rate, gas mass, or dust temperature has been observed. If CO is in a more thermalized state in the densest systems, the r_{31} ratio will decrease, resulting in lower inferred α_{CO} values based on the inferred molecular gas mass. Although there is some evidence for a higher r_{31} in denser galaxies (Daddi et al. 2015), and observations of two $z \sim 2$ PHIBSS galaxies measure r_{31} of close to unity (Bolatto et al. 2015), the thermalized limit of $r_{31} = 1$ restricts this effect to a factor of 2, not enough to fully explain the factor of ~ 5 discrepancy between the PHIBSS α_{CO} values and those in similarly dense local ULIRGs.

5.2 Resolution Effects

Another explanation for the results in Section 4 is that our measurements of Σ_{tot} are not accurate representations of the molecular gas environment within our galaxy sample. Previous studies that find a reduction in α_{CO} with increasing Σ_{tot} resolve kpc-scale regions within nearby galaxies (Sandstrom et al. 2013; Papadopoulos et al. 2012b), whereas our measurements of α_{CO} and Σ_{tot} are integrated over the entire system. As a result, our Σ_{tot} determination would fail to describe molecular gas conditions in a galaxy with significantly offset molecular gas and stellar mass distributions.

Observations of nearby galaxies, however, find that the distributions of molecular gas and stellar mass are remarkably similar. For example, Regan et al. (2001) and Leroy et al. (2008) construct high-resolution maps of CO emission in 15 and 23 nearby galaxies, respectively; both find that the CO scale length is consistent with the stellar scale length for a wide range of galaxy types. Tacconi et al. (2013) arrive at the same result (albeit with lower-resolution observations) for 21 high- z star-forming galaxies with spatially-resolved CO maps from PHIBSS, including a subset of the sources in our high- z sample (see also Genzel et al. 2013; Freundlich et al. 2013). The molecular gas distributions within nuclear starbursts, such as those observed in local ULIRGs, on the other

hand, clearly do not match their stellar distributions. Further verification that molecular gas at intermediate redshift does not live in preferentially dense environments is possible via high-resolution observations with ALMA, which – in its most extended configuration – is capable of resolving the CO $J=(3 \rightarrow 2)$ emission on \sim kpc scales at $z \sim 1$. A high-resolution census of the molecular gas in typical star-forming systems with ALMA (or NOEMA) would provide a better measurement of the total mass surface density within molecular clouds, thereby serving as a valuable check of our results.

5.3 Metallicity Effects

As discussed in Section 1, along with total surface mass density, metallicity is the galaxy property most associated with variation in α_{CO} . The dependence of α_{CO} on metallicity is driven by the underlying correlation between the fraction of CO-dark gas within a molecular cloud and extinction, which in turn depends on metallicity such that as gas-phase metallicity increases, α_{CO} decreases. Different parameterizations exist describing the dependence of α_{CO} on metallicity. For example, Narayanan et al. (2012) arrive at $\alpha_{\text{CO}} \propto 1/Z'$ as a fit to hydrodynamic simulations, while Bolatto, Wolfire & Leroy (2013), following the analytic arguments of Wolfire, Hollenbach & McKee (2010), give $\alpha_{\text{CO}} \propto \exp(0.4/Z')$, where Z' is the metallicity as a fraction of solar. Both of these parameterizations provide a good fit to observations of α_{CO} and gas-phase metallicity which indicate that on average α_{CO} decreases by roughly 1 dex over the range $8 < 12 + \log(\text{O}/\text{H}) < 9$.

Since neither direct- T nor strong-line metallicity measurements are available throughout our sample, we estimate the gas-phase metallicity of each galaxy in PHIBSS and COLD GASS according to the observed stellar mass, using an assumed mass-metallicity relation. Metallicities are first determined from the redshift-dependent mass-metallicity relation of Zahid et al. (2014), and then converted to the metallicity scale of Kobulnicky & Kewley (2004) using the conversion from Kewley & Ellison (2008). This conversion allows us to compare our results with measurements of local disks in the Sandstrom et al. (2013) sample and local dwarfs as measured by Leroy et al. (2011).

Figure 7 shows the relationship between α_{CO} and metallicity in both the low- and high- z samples. Overall, our measurements are in line with the weak negative correlation between α_{CO} and metallicity predicted. While we are unable to disentangle the contributions of Z' and Σ_{tot} in setting α_{CO} for our observed galaxy sample, the expected dependence of α_{CO} on Z' suggests that metallicity has a limited effect on our results, and in particular, would not cancel an existing trend between α_{CO} and Σ_{tot} . High-density galaxies tend to be more massive, and thus more metal rich, with lower α_{CO} values than their low-metallicity counterparts. Therefore, any underlying dependence of α_{CO} on Z' would serve to strengthen any existing anti-correlation between α_{CO} and Σ_{tot} . Moreover, the relatively weak dependence of α_{CO} on metallicity in the metal-rich regime, combined with the small range of metallicities spanned by our sample, suggests that this effect should lower α_{CO} by at most 0.13 dex across our high- z sample and 0.12 dex across our low- z sample. This small decrease is certainly less important in setting α_{CO} than the decrease in α_{CO} expected for a galaxy with a large fraction of its gas in a ULIRG-like diffuse cloud. While the presence of low-metallicity gas can significantly alter α_{CO} , the magnitude and direction of this effect in our sample are incompatible with a scenario in which the results in Sec. 4 are explained as the combination of a density effect and a metallicity effect.

Given the range of stellar mass dependencies among our depletion time models, it is unsurprising that we observe varying relationships between α_{CO} and metallicity in Fig. 7. For depletion time models TM+ and T*, we see no significant correlation between α_{CO} and metallicity. For model TZ, there is a slight negative trend between α_{CO} and metallicity ($\log \alpha_{\text{CO}} - \log Z'$ slope = -3.4 ± 0.9), while model TM- results in a very steep relationship between α_{CO} and metallicity (slope = -6.5 ± 0.9). By inferring Z' from the observed stellar mass, our metallicity estimates are highly uncertain, so as to potentially smear out an underlying $\alpha_{\text{CO}} - Z'$ trend. However, use of strong-line metallicity measurements, available for a subset of our low- z sample (Tremonti et al. 2004), results in a generally flatter $\alpha_{\text{CO}} - Z'$ relation with comparable scatter.

As shown in Fig. 7, all depletion time models, except for TM-, are consistent with the weak negative correlation between α_{CO} and metallicity observed locally in the relevant metallicity range. While the points for model T* are higher at $z \sim 1$ than $z \sim 0$, their slope is still consistent with the expected Z' dependence. The nature of this general evolution in α_{CO} is unclear. As discussed in Section 5.5, uncertainties in the redshift evolution of t_{dep} result in uncertainties in the normalization of our high- z α_{CO} values. Relative differences in α_{CO} as a function of galaxy properties, however, are not subject to this same uncertainty. Regardless, the strong anti-correlation we find for model TM- is inconsistent with the expected Z' dependence, such that model TM- is incompatible with the COLD GASS and PHIBSS observations. Alternatively, the weak correlation between α_{CO} and metallicity in models TZ, TM+, and T*, corresponding to a decrease in α_{CO} of around 0.2 dex across our sample, is consistent with local observations and models, providing further evidence in support of these depletion time models.

5.4 Surface Density Dependent t_{dep} Models

While the depletion time models we adopt do not necessarily preclude a correlation between t_{dep} and total mass surface density, some studies report a more direct relationship between depletion time and surface density. For example, a Kennicutt-Schmidt (KS) law ($\Sigma_{\text{SFR}} \propto \Sigma_{\text{mol gas}}^N$) with $N = 1.4$ (Kennicutt 1998) or a model relating t_{dep} to the orbital time of the gas (Kennicutt 1998; Kennicutt et al. 2007) or stellar surface density (Boselli et al. 2014) all imply strong correlations between t_{dep} and total mass surface density. Given that our α_{CO} estimates are determined directly from depletion time models (Eq. 8), a model that assumes a correlation between t_{dep} and surface density will undoubtedly imply a trend between α_{CO} and total mass surface density.

To demonstrate the extent of the effect produced by adopting one of these models, we show the relationship between Σ_{tot} and α_{CO} determined from an $N = 1.4$ KS law in Fig. 8. In this case, a stronger relationship between α_{CO} and surface density is observed, consistent with a $\sim 20\%$ diffuse fraction at low- z and a $\sim 10\%$ diffuse fraction at high- z (contributing $\sim 41\%$ and $\sim 24\%$ to the CO luminosity at low- and high- z respectively). The small change between these results and the results presented in Sec. 4 is likely due to the fact that molecular gas (controlling the density effect) represents a sub-dominant mass component within our systems. If N is chosen to be less than 1.4 (in line with more recent results, e.g. Genzel et al. 2010), the relationship between α_{CO} and Σ_{tot} flattens, better matching the trend expected for a $\lesssim 10\%$ diffuse fraction for both samples. While the adoption of an $N > 1.4$ KS law would increase the inferred diffuse fraction, most measurements of N within nearby galaxies lie between 1 (Leroy et al. 2008; Bigiel et al. 2008, 2011; Schrubba et al. 2011) and 1.4 (Kennicutt 1998;

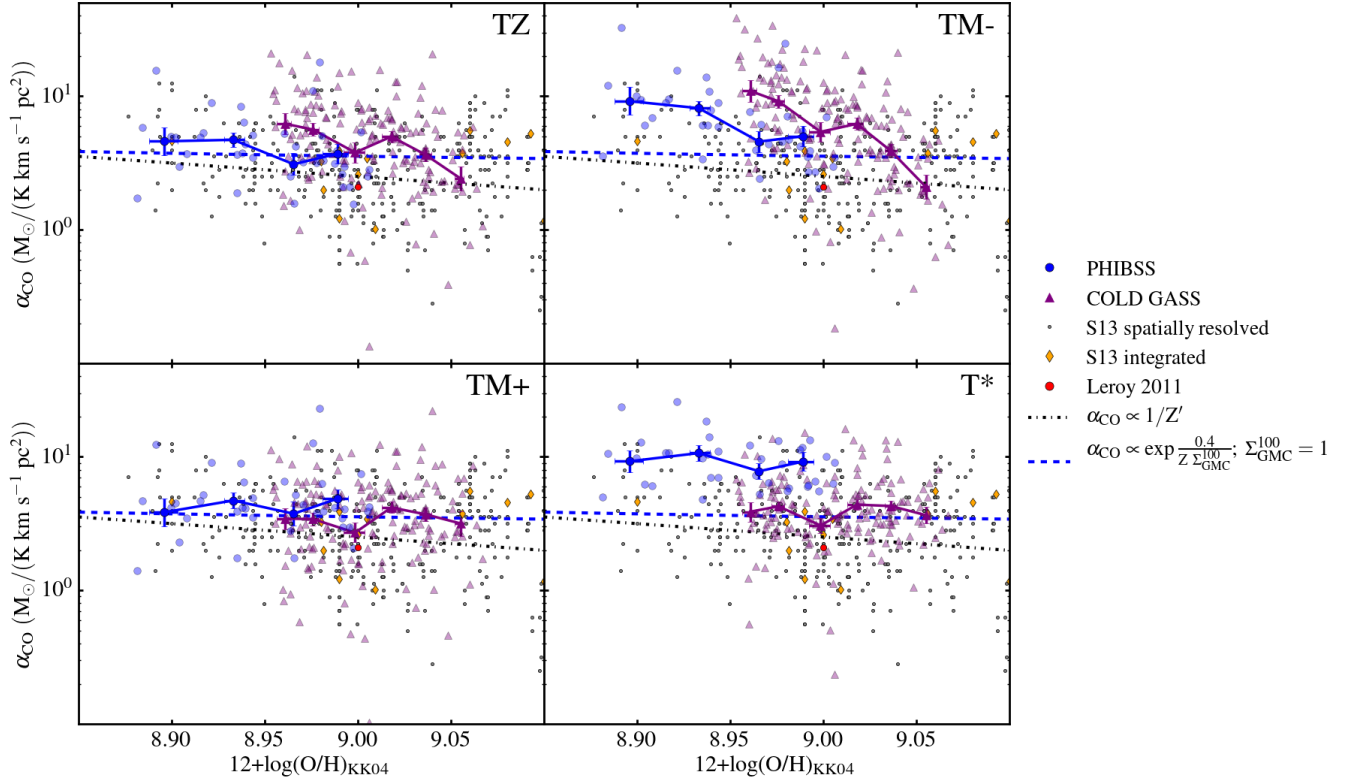


Figure 7. The dependence of α_{CO} on metallicity in both the low- and high- z samples in our study. Blue, purple, grey, and orange points are the same as in Figures 5 and 6. Red points are taken from measurements within the Local Group from Leroy et al. (2011). Two models for the dependence of α_{CO} on metallicity are also shown: the blue dashed line shows the weak dependence of α_{CO} on metallicity given in Bolatto, Wolfire & Leroy (2013), and the black dot-dashed line shows the stronger dependence given by Narayanan et al. (2012). Both the low- and high- z samples qualitatively match the expected relationship between α_{CO} and metallicity in all t_{dep} models except TM-. Additionally, the scatter in our measurements at fixed metallicity is similar to that of Sandstrom et al. (2013).

Krumholz, McKee & Tumlinson 2009; Kennicutt & Evans 2012), and CO-independent measurements within local galaxies find N to be consistent with 1 (Leroy et al. 2013). Furthermore, if we take t_{dep} to be proportional to the orbital time of the gas (Kennicutt 1998), determined from the HI line width, the relationship between α_{CO} and Σ_{tot} matches the trend observed using the $N = 1.4$ KS law in the low- z sample. In the high- z sample, HI orbital velocities are not available and there is no evidence that the CO line width is dominated by clear rotational motions, so we do not test this case. Although the adoption of a t_{dep} model that strongly correlates with surface density results in a stronger correlation between α_{CO} and Σ_{tot} within our sample, the relationship between α_{CO} and total mass surface density, indicative of the overall structure of molecular gas within galaxies, does not change between the low- z and high- z samples. Specifically, our analysis indicates that molecular gas, both at low- and high- z , is primarily distributed among self-gravitating GMCs and not large, diffuse clouds.

5.5 Evolution of t_{dep}

The nature of the star-formation process at high- z , which is directly connected to the $z \sim 1$ depletion time, is the subject of considerable debate. We have adopted forms of t_{dep} that evolve slowly with redshift, consistent with qualitatively non- (or weakly-) evolving star-formation process, motivated by many different CO-based observations (Bauermeister et al. 2013a; Geach et al. 2011; Saintonge et al. 2013; Magdis et al. 2012b; Genzel et al. 2015). Specifically,

Genzel et al. (2015), using both dust- and CO-based gas measurements, find that depletion times evolve weakly with redshift for galaxies on the star-forming main sequence. In contrast, Scoville et al. (2016), using stacked far-IR photometry of galaxies at $z > 1$, measure depletion times on the order of 10^8 yrs, at least a factor of 5 below the $z \sim 1$ depletion times that we adopt. Such a remarkably short depletion time implies that star formation at $z \sim 1$ is more similar to that occurring in local ULIRGs than in the Milky Way.

Our primary results, which show α_{CO} to be independent of Σ_{tot} at $z \sim 0$ and $z \sim 1$, are largely insensitive to the assumed evolution of t_{dep} . Whereas depletion times as low as 10^8 yrs result in α_{CO} values close to those of local ULIRGs, they only affect the normalization of our measurements, leaving the lack of a significant trend between α_{CO} and Σ_{tot} unexplained. On the other hand, the motivation for lowering α_{CO} in high-surface-density galaxies at $z \sim 1$ may not apply for our sample. While kpc-scale clumps of star-formation activity have been observed in high- z galaxies (Förster Schreiber et al. 2011; Genzel et al. 2011), it is possible that these star-forming clumps are composed of a collection of GMCs (see Hemmati et al. 2014). In addition, although a variety of star formation histories have been shown to be consistent with the observed star-forming main sequence (Kelson 2014; Abramson et al. 2015), depletion times as low as 10^8 years require an extremely unlikely conspiracy of gas accretion and cooling to avoid conflict with the low scatter in the main sequence at $z > 1$ (Speagle et al. 2014). As we do not observe a trend between α_{CO} and Σ_{tot} , our observations indicate that molecular gas in typical star-forming galaxies at

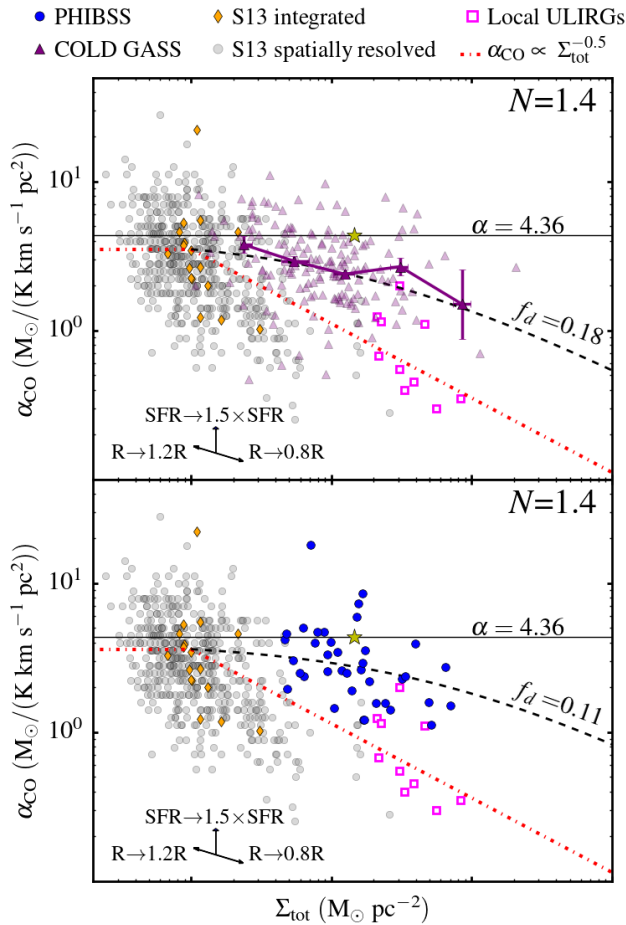


Figure 8. The relationship between α_{CO} and surface density assuming an $N = 1.4$ Kennicutt-Schmidt law. Blue, purple, grey, and orange points are the same as in Figures 5 and 6. As in Figures 5 and 6, the model from Bolatto, Wolfire & Leroy (2013) is illustrated as the red dot-dashed line, and the expected trends between α_{CO} and Σ_{tot} for galaxies containing 18% and 11% diffuse gas are shown as the black dashed lines at low and high z respectively. Adopting this surface-density dependent depletion time, a strong correlation between α_{CO} and Σ_{tot} is observed, consistent with a non-negligible fraction of molecular gas in the diffuse phase. The relationship between α_{CO} and surface density does not change between the $z \sim 1$ and $z \sim 0$ samples, however. Thus, even if the depletion time is strongly correlated with surface density, we find no evidence of that the structure of molecular gas within ‘typical’ star-forming galaxies is significantly different at $z \sim 1$ compared with $z \sim 0$.

$z < 1.5$ largely resides in self-gravitating GMCs with a Milky Way α_{CO} value. This molecular gas structure, together with the high- z CO observations, implies a weakly evolving t_{dep} across cosmic time.

6 CONCLUSIONS

For a sample of 164 low- z and 38 high- z star-forming galaxies with CO detections drawn from COLD GASS and PHIBSS, respectively, we estimate the CO-H₂ conversion factor (α_{CO}) using the observed star formation rate and an adopted depletion time (t_{dep}) to infer the molecular gas mass. In particular, we study the relationship between α_{CO} and total mass surface density (Σ_{tot}), constrain-

ing the structure of molecular gas over cosmic time. Our primary conclusions are as follows:

- For a broad range of assumed depletion times, we do not find a significant correlation between α_{CO} and total mass surface density for both our low- z and high- z samples, which suggests that $\lesssim 10\%$ of the molecular gas (by mass; $\lesssim 30\%$ by luminosity) in these systems is contained in diffuse clouds, akin to those that populate local ULIRGs. Instead, we find that the molecular content of typical star-forming galaxies at $z < 1.5$ is primarily comprised of self-gravitating GMCs, with an α_{CO} value comparable to that found in the Milky Way.
- For both our low- z and high- z samples, which primarily include metal-rich systems, we find that the relationship between α_{CO} and gas-phase metallicity is consistent with the weak negative correlation observed locally. As this relationship is driven by gas chemistry within molecular clouds, the constancy of this relationship is evidence that the small-scale physics of GMC collapse at $z \sim 1$ is similar to that locally, despite potential differences in large-scale ISM conditions.
- Altogether, our analysis points to a molecular gas depletion time that is weakly evolving with redshift, such that typical star-forming galaxies at $z > 1$ are more similar to scaled-up Milky Way-like systems than local ULIRGs.

ACKNOWLEDGEMENTS

We are grateful to the anonymous referee, whose comments significantly improved the clarity of this work.

Support for this work was provided by NASA through grants (GO-12547 and AR-13242) from the Space Telescope Science Institute, which is operated by the Association of Universities for Research in Astronomy, Inc., under NASA contract NAS 5-26555. This work was also supported, in part, by NSF grant AST-1518257. TC and MCC thank the National Achievement Rewards for College Scientists (ARCS) Foundation and the International Space Science Institute (ISSI), respectively, for support of this work. The observations presented here would not have been possible without the diligence and sensitive new generation receivers from the IRAM staff - for this they have our highest admiration and thanks. We also thank the astronomers on duty and telescope operators for delivering consistently high quality data to our team.

Funding for SDSS-III has been provided by the Alfred P. Sloan Foundation, the Participating Institutions, the National Science Foundation, and the U.S. Department of Energy Office of Science. The SDSS-III web site is <http://www.sdss3.org/>.

SDSS-III is managed by the Astrophysical Research Consortium for the Participating Institutions of the SDSS-III Collaboration including the University of Arizona, the Brazilian Participation Group, Brookhaven National Laboratory, Carnegie Mellon University, University of Florida, the French Participation Group, the German Participation Group, Harvard University, the Instituto de Astrofísica de Canarias, the Michigan State/Notre Dame/JINA Participation Group, Johns Hopkins University, Lawrence Berkeley National Laboratory, Max Planck Institute for Astrophysics, Max Planck Institute for Extraterrestrial Physics, New Mexico State University, New York University, Ohio State University, Pennsylvania State University, University of Portsmouth, Princeton University, the Spanish Participation Group, University of Tokyo, Uni-

versity of Utah, Vanderbilt University, University of Virginia, University of Washington, and Yale University.

This research has made use of the NASA/IPAC Extragalactic Database (NED) which is operated by the Jet Propulsion Laboratory, California Institute of Technology, under contract with the National Aeronautics and Space Administration.

This research made use of *Astropy*, a community-developed core Python package for Astronomy (Astropy Collaboration et al. 2013). Additionally, the Python packages *NumPy* (Walt, Colbert & Varoquaux 2011), *iPython* (Perez & Granger 2007), *SciPy* (Jones et al. 2001), and *matplotlib* (Hunter 2007) were utilized for the majority of our data analysis and presentation. This work has made use of the Rainbow Cosmological Surveys Database, which is operated by the Universidad Complutense de Madrid (UCM), partnered with the University of California Observatories at Santa Cruz (UCO/Lick, UCSC), as well as the NASA/IPAC Extragalactic Database (NED) which is operated by the Jet Propulsion Laboratory, California Institute of Technology, under contract with the National Aeronautics and Space Administration.

REFERENCES

- Aaronson M., Olszewski E. W., 1984, *Nature*, 309, 414
- Abramson L. E., Gladders M. D., Dressler A., Oemler, Jr. A., Pogianti B., Vulcani B., 2015, *ApJ*, 801, L12
- Ackermann M. et al., 2012, *ApJ*, 755, 22
- Ade P. A. R. et al., 2011, *A&A*, 536, A19
- Alam S. et al., 2015, *ApJS*, 219, 12
- Astropy Collaboration et al., 2013, *A&A*, 558, A33
- Barro G. et al., 2011, *ApJS*, 193, 13
- Bauermeister A. et al., 2013a, *ApJ*, 768, 132
- Bauermeister A., Blitz L., Bolatto A., Bureau M., Teuben P., Wong T., Wright M., 2013b, *ApJ*, 763, 64
- B  thermin M. et al., 2015, *A&A*, 573, A113
- B  thermin M. et al., 2016, *A&A*, 586, L7
- Bigiel F., Leroy A., Walter F., Brinks E., de Blok W. J. G., Madore B., Thornley M. D., 2008, *AJ*, 136, 2846
- Bigiel F. et al., 2011, *ApJ*, 730, L13
- Bolatto A. D., Leroy A. K., Rosolowsky E., Walter F., Blitz L., 2008, *ApJ*, 686, 948
- Bolatto A. D. et al., 2015, *ApJ*, 809, 175
- Bolatto A. D., Wolfire M., Leroy A. K., 2013, *ARA&A*, 51, 207
- Boselli A., Cortese L., Boquien M., Boissier S., Catinella B., Lagos C., Saintonge A., 2014, *A&A*, 564, A66
- Brammer G. B. et al., 2012, *ApJS*, 200, 13
- Brinchmann J., Charlot S., White S. D. M., Tremonti C., Kauffmann G., Heckman T., Brinkmann J., 2004, *MNRAS*, 351, 1151
- Carilli C. L., Walter F., 2013, *ARA&A*, 51, 105
- Catinella B. et al., 2010, *MNRAS*, 403, 683
- Ceverino D., Dekel A., Bournaud F., 2010, *MNRAS*, 404, 2151
- Chabrier G., 2003, *PASP*, 115, 763
- Cooper M. C. et al., 2011, *ApJS*, 193, 14
- Cooper M. C. et al., 2012, *MNRAS*, 419, 3018
- Daddi E. et al., 2010, *ApJ*, 713, 686
- Daddi E. et al., 2015, *A&A*, 577, A46
- Daddi E. et al., 2007, *ApJ*, 670, 156
- Dav   R., Finlator K., Oppenheimer B. D., 2012, *MNRAS*, 421, 98
- Davis M. et al., 2007, *ApJ*, 660, L1
- Dickman R. L., 1978, *ApJS*, 37, 407
- Dickman R. L., Snell R. L., Schloerb F. P., 1986, *ApJ*, 309, 326
- Downes D., Solomon P. M., 1998, *ApJ*, 507, 615
- Dunne L. et al., 2011, *MNRAS*, 417, 1510
- Elbaz D. et al., 2007, *A&A*, 468, 33
- Elbaz D. et al., 2011, *A&A*, 533, A119
- Elbaz D. et al., 2010, *A&A*, 518, L29
- F  rster Schreiber N. M. et al., 2009, *ApJ*, 706, 1364
- F  rster Schreiber N. M. et al., 2011, *ApJ*, 739, 45
- Frerking M. A., Langer W. D., Wilson R. W., 1982, *ApJ*, 262, 590
- Freundlich J. et al., 2013, *A&A*, 553, A130
- Geach J. E., Smail I., Moran S. M., MacArthur L. A., Lagos C. d. P., Edge A. C., 2011, *ApJ*, 730, L19
- Genzel R. et al., 2011, *ApJ*, 733, 101
- Genzel R. et al., 2012, *ApJ*, 746, 69
- Genzel R. et al., 2010, *MNRAS*, 407, 2091
- Genzel R. et al., 2013, *ApJ*, 773, 68
- Genzel R. et al., 2015, *ApJ*, 800, 20
- Griffith R. L. et al., 2012, *ApJS*, 200, 9
- Grogin N. A. et al., 2011, *ApJS*, 197, 35
- Hao C.-N., Kennicutt R. C., Johnson B. D., Calzetti D., Dale D. A., Moustakas J., 2011, *ApJ*, 741, 124
- Hemmati S. et al., 2014, *ApJ*, 797, 108
- Huang M.-L., Kauffmann G., 2014, *MNRAS*, 443, 1329
- Hunter J. D., 2007, *Computing in Science & Engineering*, 9, 90
- Ilbert O. et al., 2010, *ApJ*, 709, 644
- Israel F. P., 1997, *A&A*, 328, 471
- Iverson R. J. et al., 2012, *MNRAS*, 425, 1320
- Jones E., Oliphant T., Peterson P., et al., 2001, *SciPy: Open source scientific tools for Python*. [Online; accessed 2016-07-03]
- Kamenetzky J., Rangwala N., Glenn J., Maloney P. R., Conley A., 2014, *ApJ*, 795, 174
- Kauffmann G. et al., 2003, *MNRAS*, 341, 33
- Kelson D. D., 2014, *ArXiv*: 1406.5191
- Kennicutt R. C. et al., 2011, *PASP*, 123, 1347
- Kennicutt R. C., Evans N. J., 2012, *ARA&A*, 50, 531
- Kennicutt, Jr. R. C., 1998, *ApJ*, 498, 541
- Kennicutt, Jr. R. C. et al., 2003, *PASP*, 115, 928
- Kennicutt, Jr. R. C. et al., 2007, *ApJ*, 671, 333
- Kewley L. J., Ellison S. L., 2008, *ApJ*, 681, 1183
- Kobulnicky H. A., Kewley L. J., 2004, *ApJ*, 617, 240
- Koekemoer A. M. et al., 2011, *ApJS*, 197, 36
- Krumholz M. R., McKee C. F., Tumlinson J., 2009, *ApJ*, 699, 850
- Krumholz M. R., Thompson T. A., 2007, *ApJ*, 669, 289
- K  mmel M., Walsh J. R., Pirzkal N., Kuntschner H., Pasquali A., 2009, *PASP*, 121, 59
- Leroy A. K. et al., 2011, *ApJ*, 737, 12
- Leroy A. K. et al., 2015, *ApJ*, 801, 25
- Leroy A. K. et al., 2009, *AJ*, 137, 4670
- Leroy A. K., Walter F., Brinks E., Bigiel F., de Blok W. J. G., Madore B., Thornley M. D., 2008, *AJ*, 136, 2782
- Leroy A. K. et al., 2013, *AJ*, 146, 19
- Lilly S. J., Le Fevre O., Hammer F., Crampton D., 1996, *ApJ*, 460, L1
- Lotz J. M. et al., 2008, *ApJ*, 672, 177
- Madau P., Dickinson M., 2014, *ARA&A*, 52, 415
- Madau P., Ferguson H. C., Dickinson M. E., Giavalisco M., Steidel C. C., Fruchter A., 1996, *MNRAS*, 283, 1388
- Magdis G. E. et al., 2012a, *ApJ*, 760, 6
- Magdis G. E. et al., 2011, *ApJ*, 740, L15
- Magdis G. E. et al., 2012b, *ApJ*, 758, L9
- Magnelli B., Elbaz D., Chary R. R., Dickinson M., Le Borgne D., Frayer D. T., Willmer C. N. A., 2011, *A&A*, 528, A35
- Magnelli B. et al., 2014, *A&A*, 561, A86

- Martig M., Bournaud F., Teyssier R., Dekel A., 2009, *ApJ*, 707, 250
- Mauersberger R., Henkel C., Walsh W., Schulz A., 1999, *A&A*, 341, 256
- McKee C. F., Ostriker E. C., 2007, *ARA&A*, 45, 565
- Messias H. et al., 2014, *A&A*, 568, A92
- Narayanan D., Krumholz M., Ostriker E. C., Hernquist L., 2011, *MNRAS*, 418, 664
- Narayanan D., Krumholz M. R., Ostriker E. C., Hernquist L., 2012, *MNRAS*, 421, 3127
- Nelson E. J. et al., 2012, *ApJ*, 747, L28
- Newman J. A. et al., 2013, *ApJS*, 208, 5
- Noeske K. G. et al., 2007, *ApJ*, 660, L43
- Oka T., Hasegawa T., Sato F., Tsuboi M., Miyazaki A., Sugimoto M., 2001, *ApJ*, 562, 348
- Papadopoulos P. P., van der Werf P., Xilouris E., Isaak K. G., Gao Y., 2012a, *ApJ*, 751, 10
- Papadopoulos P. P., van der Werf P. P., Xilouris E. M., Isaak K. G., Gao Y., Mühle S., 2012b, *MNRAS*, 426, 2601
- Papovich C. et al., 2016, *ArXiv*: 1610.05313
- Pérez-González P. G., Trujillo I., Barro G., Gallego J., Zamorano J., Conselice C. J., 2008, *ApJ*, 687, 50
- Pettini M., Pagel B. E. J., 2004, *MNRAS*, 348, L59
- Prez F., Granger B. E., 2007, *Computing in Science & Engineering*, 9, 21
- Reddy N. A., Steidel C. C., Pettini M., Adelberger K. L., Shapley A. E., Erb D. K., Dickinson M., 2008, *ApJS*, 175, 48
- Regan M. W., Thornley M. D., Helfer T. T., Sheth K., Wong T., Vogel S. N., Blitz L., Bock D. C.-J., 2001, *ApJ*, 561, 218
- Rodighiero G. et al., 2011, *ApJ*, 739, L40
- Saintonge A. et al., 2011a, *MNRAS*, 415, 32
- Saintonge A. et al., 2011b, *MNRAS*, 415, 61
- Saintonge A. et al., 2013, *ApJ*, 778, 2
- Saintonge A. et al., 2012, *ApJ*, 758, 73
- Sanders D. B., Mirabel I. F., 1996, *ARA&A*, 34, 749
- Sandstrom K. M. et al., 2013, *ApJ*, 777, 5
- Santini P. et al., 2014, *A&A*, 562, A30
- Schinnerer E., Weiß A., Aalto S., Scoville N. Z., 2010, *ApJ*, 719, 1588
- Schruba A. et al., 2011, *AJ*, 142, 37
- Scoville N. et al., 2016, *ApJ*, 820, 83
- Sersic J. L., 1968, *Atlas de galaxies australes*
- Sodroski T. J. et al., 1995, *ApJ*, 452, 262
- Solomon P. M., Downes D., Radford S. J. E., Barrett J. W., 1997, *ApJ*, 478, 144
- Solomon P. M., Rivolo A. R., Barrett J., Yahil A., 1987, *ApJ*, 319, 730
- Speagle J. S., Steinhardt C. L., Capak P. L., Silverman J. D., 2014, *ApJS*, 214, 15
- Spilker J. S. et al., 2015, *ApJ*, 811, 124
- Strong A. W., Moskalenko I. V., Reimer O., Digel S., Diehl R., 2004, *A&A*, 422, L47
- Tacconi L. J. et al., 2010, *Nature*, 463, 781
- Tacconi L. J. et al., 2008, *ApJ*, 680, 246
- Tacconi L. J. et al., 2006, *ApJ*, 640, 228
- Tacconi L. J. et al., 2013, *ApJ*, 768, 74
- Tamura Y., Saito T., Tsuru T. G., Uchida H., Iono D., Yun M. S., Espada D., Kawabe R., 2014, *ApJ*, 781, L39
- Tremonti C. A. et al., 2004, *ApJ*, 613, 898
- Twite J. W., Conselice C. J., Buitrago F., Noeske K., Weiner B. J., Acosta-Pulido J. A., Bauer A. E., 2012, *MNRAS*, 420, 1061
- van der Wel A. et al., 2014, *ApJ*, 788, 28
- van Dokkum P., Brammer G., Momcheva I., Skelton R. E., Whitaker K. E., for the 3D-HST team, 2013, *ArXiv*: 1305.2140
- Walt S. v. d., Colbert S. C., Varoquaux G., 2011, *Computing in Science & Engineering*, 13, 22
- Walter F., Brinks E., de Blok W. J. G., Bigiel F., Kennicutt, Jr. R. C., Thornley M. D., Leroy A., 2008, *AJ*, 136, 2563
- Wang R. et al., 2013, *ApJ*, 773, 44
- Whitaker K. E., van Dokkum P. G., Brammer G., Franx M., 2012, *ApJ*, 754, L29
- Wolfire M. G., Hollenbach D., McKee C. F., 2010, *ApJ*, 716, 1191
- Wuyts S. et al., 2012, *ApJ*, 753, 114
- Wuyts S. et al., 2011, *ApJ*, 738, 106
- Yao L., Seaquist E. R., Kuno N., Dunne L., 2003, *ApJ*, 588, 771
- York D. G. et al., 2000, *AJ*, 120, 1579
- Zahid H. J., Dima G. I., Kudritzki R.-P., Kewley L. J., Geller M. J., Hwang H. S., Silverman J. D., Kashino D., 2014, *ApJ*, 791, 130
- Zahid H. J., Geller M. J., Kewley L. J., Hwang H. S., Fabricant D. G., Kurtz M. J., 2013, *ApJ*, 771, L19
- Zibetti S., Charlot S., Rix H.-W., 2009, *MNRAS*, 400, 1181